were approved by the Kyoto University Animal Care Committee. Female C3H/He mice and BALB/c *nu/nu* mice at 5 weeks of age were purchased from Japan SLC (Hamamatsu, Japan). FM3A and Suit2/Luc tumour models were prepared as described in a previous report [9]. The cells were subcutaneously implanted in the right thigh, except in the mice that were to be used for the bioluminescence imaging in which the cells were subcutaneously implanted in both thighs. After tumour implantation, mice were fed an AIN76-A-based, biotin-free diet (Oriental Yeast Company, Tokyo, Japan) in order to prevent dietary biotin from inhibiting the binding of $^{125}$I-IBB to POS. The mice were subjected to a tracer study 2 weeks after implantation. The average diameter and average volume of the tumours were 8 mm and 350 mm$^3$, respectively.

### Biodistribution

$^{125}$I-IBB (37 kBq) was injected intravenously into FM3A-implanted mice ($n$=3–5), and at 1, 3, 6 and 24 h after injection, the mice were killed. For the pretargeting study, the mice ($n$=5) were injected with 30 μg of POS and 24 h later $^{125}$I-IBB was injected intravenously. The mice were killed at the same time points as above. Whole organs were immediately removed and weighed, and their radioactivity was measured with an autowell gamma counter (ARC2000; Aloka, Tokyo, Japan). The results are expressed in terms of the percent injected dose per gram of tissue (%ID/g).

### In vivo blocking study

FM3A-implanted mice ($n$=5) were pretargeted with POS (30 μg); 24 h later, $^{125}$I-IBB (37 kBq) was injected intravenously, with or without D-biotin (1 nmol) or with unlabelled IBB (500 pmol). Six hours after $^{125}$I-IBB administration, the mice were killed. Whole organs were immediately removed and weighed, and their radioactivity was measured with the gamma counter (ARC2000). The results are expressed as %ID/g.

### Size-exclusion analysis of radioactive compounds in tumours

FM3A-implanted mice ($n$=5) were pretargeted with POS (30 μg), and 24 h later, $^{125}$I-IBB (8.0 MBq) was injected intravenously. The mice were killed 6 h after the injection of $^{125}$I-IBB, and the tumours were removed. Extracts were prepared according to a previously reported method [18], with slight modification. In brief, the tumours were homogenized in ice-cold 0.1 *M* Tris-HCl buffer containing 0.15 *M* NaCl (pH 6.5), using a Polytron homogenizer (PT10-35, Kinematica, Switzerland). The preparations were then centrifuged at 4°C and 5,000×*g* for 30 min (Micro Cooling Centrifuge 5922; Kubota, Osaka, Japan). The supernatants were filtered through a 0.46-μm filter (Nacalai Tesque, Kyoto, Japan) and analysed by size-exclusion chromatography using a PD-10 column (GE Healthcare Bioscience).

### In vivo imaging

A SPECT-2000H scanner (Hitachi Medical, Tokyo, Japan) equipped with a low-energy, high-resolution, parallel-hole collimator [19, 20] was used. For direct targeting ($n$=4), $^{123}$I-IPOS (30 μg, 4.9–7.4 MBq) was injected intravenously into each FM3A-implanted mouse. For the pretargeting method ($n$=5), $^{123}$I-IBB (3.1–16 MBq) was injected into a tail vein 24 h after pretargeting with POS (30 μg). Under 2.5% halothane anaesthesia, the mice were placed on a scanner bed in the prone position. Planar images were obtained at 24 h after the injection of $^{123}$I-IPOS in mice in the direct-targeted group or at 6 h after the injection of $^{123}$I-IBB in mice in the pretargeted group. The image acquisition time was 10 min for both the groups. Regions of interest (ROI) were set on the tumour in the right thigh and the corresponding area in the left thigh.

### Comparison between $^{125}$I-IBB accumulation and HIF-1 transcriptional activity in the same tumours in mice pretargeted with POS

The Suit2/Luc-implanted mice ($n$=5) were pretargeted with POS (30 μg) and 24 h later, $^{125}$I-IBB (37 kBq) was injected intravenously. After 5.5 h, 200 μl of D-luciferin solution (10 mg/ml in PBS; VivoGlo Luciferin, Promega, WI) was injected intraperitoneally. After 20 min, the mice were anaesthetized with 2.5% isoflurane and imaged according to a previously described method [9]. After bioluminescence imaging, the mice were killed and the radioactivity in each tumour was measured.

### Autoradiography

Autoradiographic studies were performed in Suit2/Luc-implanted mice ($n$=6). The mice were pretargeted with POS (30 μg) and 24 h later, $^{125}$I-IBB (4.1 MBq) was injected intravenously. After another 4 h, pimonidazole (PIMO, 60 mg/kg) was injected intraperitoneally and the mice were killed 2 h later. Autoradiograms were then obtained and analysed according to a previously described method [19–21]. The adjacent section on each autoradiogram was stained with haematoxylin-eosin to identify regions of necrosis.

### Immunohistochemistry

The slides used in the autoradiographic study were subjected to dual fluorescent immunostaining for HIF-1α

and PIMO. The sections were fixed in 2% paraformaldehyde and ice-cold methanol, blocked with Protein Block Serum Free (Dako, Glostrup, Denmark), and treated with anti-human/mouse HIF-1α polyclonal antibody (R&D Systems, Minneapolis, MN) as a primary antibody. The specific signals were detected using an Alexa Fluor 568-conjugated $F(ab')_2$ fragment of goat anti-rabbit antibody (Invitrogen, San Diego, CA). Thereafter, after washing with PBS, FITC-conjugated mouse $IgG_1$ monoclonal antibody (Chemicon, Temecula, CA) was treated according to the manufacturer's protocol for PIMO staining. The sections were then dried and coverslipped using an antifade reagent (ProLong Gold; Invitrogen). To evaluate the specificity of the HIF-1α signal, negative control rabbit immunoglobulin (Dako) was incubated with the adjacent sections, instead of the primary antibody. To evaluate the specificity of the PIMO signal, tumour sections derived from PIMO-untreated mice were stained following the same protocol. Fluorescent microscopic images were obtained by BIO-REVO BZ-9000 (Keyence, Osaka, Japan).

### Image analysis

The autoradiograms were quantified using MultiGauge software (ver. 3.0, Fuji Photo Film, Tokyo, Japan) and the immunohistochemical images were analysed using BZ analyser software (Keyence). ROIs were set in identical positions in both images on the basis of the x- and y-position of each ROI displayed in both software programs. The necrotic regions were excluded from the analysis. We set 10–14 ROIs (area 1 $mm^2$) on the autoradiogram of each tumour and then transferred them to the corresponding immunohistochemical image. The radioactivity in each ROI was expressed in terms of percent injected dose. The expression densities of HIF-1α and PIMO were determined in terms of the percentage of the positively stained region.

### Statistical analyses

The two groups were compared using the Mann-Whitney *U* test, and correlation coefficients were assessed using the Spearman rank analysis. A chi-squared test was used to compare the correlation coefficients between $^{125}$I-IBB accumulation and HIF-1α expression and PIMO adduct formation. Values of $p < 0.05$ were considered statistically significant.

## Results

### Radiosynthesis of $^{123/125}$I-IBB and $^{123}$I-IPOS

$^{123}$I-IBB and $^{125}$I-IBB were obtained in the absence of a carrier and with radiochemical yields of 29% and 65% and radiochemical purities of greater than 95% and greater than 94%, respectively. $^{123}$I-IPOS was obtained with a radiochemical yield of 90% and a radiochemical purity of greater than 99%.

### Biodistribution

An examination of the biodistribution of $^{125}$I-IBB alone revealed that the tumour-to-blood ratio was less than 1 at all time points. This indicated that $^{125}$I-IBB did not accumulate in the tumours. The radioactivity in the stomach was low indicating the resistance of $^{125}$I-IBB to deiodination in vivo (Table 1). In contrast, in the pretargeted group, the tumour-to-blood ratio was greater than 1 as early as 1 h after the injection of $^{125}$I-IBB and the tumour-to-blood ratio increased in a time-dependent manner (Table 2). The blood clearance in both groups was comparable. In the pretargeted group, tumour accumulation of $^{125}$I-IBB 6 h after injection was 1.58±0.42%ID/g, which was more than 30-fold higher than for $^{125}$I-IBB alone (0.05±0.01%ID/g). The radioactivity in the normal tissues decreased more rapidly than in the

**Table 1** Biodistribution of $^{125}$I-IBB in FM3A-implanted mice

| Organ | Time after injection (h) | | | |
|---|---|---|---|---|
| | 1 | 3 | 6 | 24 |
| Blood | 1.12±0.43 | 0.33±0.01 | 0.15±0.00 | 0.03±0.01 |
| Liver | 6.36±1.70 | 1.21±0.04 | 0.20±0.04 | 0.02±0.01 |
| Heart | 1.27±0.31 | 0.26±0.01 | 0.07±0.04 | 0.02±0.02 |
| Lung | 1.14±0.22 | 0.30±0.04 | 0.10±0.03 | 0.02±0.01 |
| Kidney | 5.54±0.74 | 1.06±0.23 | 0.35±0.18 | 0.07±0.02 |
| Stomach | 0.62±0.13 | 0.35±0.23 | 0.33±0.24 | 0.12±0.10 |
| Intestine | 32.61±8.24 | 24.73±12.12 | 10.69±4.93 | 0.95±0.64 |
| Tumour | 0.53±0.14 | 0.13±0.04 | 0.05±0.01 | 0.01±0.01 |
| Muscle | 0.84±0.18 | 0.15±0.05 | 0.03±0.02 | 0.01±0.01 |
| Tumour/blood ratio | 0.49±0.14 | 0.39±0.09 | 0.36±0.09 | 0.57±0.57 |

Organ uptake values are means ±SD ($n$=3–5) in units of percent injected dose per gram of tissue, except for the stomach (percent injected dose) and tumour/blood ratio

**Table 2** Biodistribution of $^{125}$I-IBB in FM3A-implanted mice pretargeted with POS

| Organ | Time after injection (h) | | | |
|---|---|---|---|---|
| | 1 | 3 | 6 | 24 |
| Blood | 1.28±0.22 | 0.58±0.05 | 0.37±0.05 | 0.05±0.01 |
| Liver | 10.16±0.98 | 5.56±0.74 | 4.07±0.38 | 0.57±0.15 |
| Heart | 1.77±0.11 | 0.90±0.12 | 0.59±0.08 | 0.06±0.02 |
| Lung | 1.98±0.24 | 0.95±0.13 | 0.67±0.07 | 0.08±0.01 |
| Kidney | 25.09±1.42 | 11.58±2.46 | 5.78±1.02 | 0.30±0.04 |
| Stomach | 0.63±0.15 | 0.56±0.17 | 0.34±0.20 | 0.08±0.05 |
| Intestine | 22.45±3.40 | 20.11±7.22 | 8.66±6.13 | 0.76±0.42 |
| Tumour | 2.73±0.67 | 2.03±0.16 | 1.58±0.42 | 0.59±0.23 |
| Muscle | 1.04±0.16 | 0.47±0.13 | 0.30±0.11 | 0.04±0.02 |
| Tumour/blood ratio | 2.15±0.39 | 3.51±0.26 | 4.23±0.81 | 13.13±4.58 |

Organ uptake values are means ±SD ($n$=5) in units of percent injected dose per gram of tissue, except for the stomach (percent injected dose) and tumour/blood ratio

tumour. The radioactivity in the tumour at 24 h after injection was the second highest among the organs examined and both the tumour-to-blood and tumour-to-muscle ratios further increased (Table 2).

Tumour uptake of $^{125}$I-IBB was significantly reduced to 46% following treatment with nonradioactive IBB (Table 3). Concomitant treatment with D-biotin also resulted in a 37% decrease in tumour uptake of $^{125}$I-IBB (data not shown). $^{125}$I-IBB accumulation in other tissues, except the blood, decreased following treatment with nonradioactive IBB.

### Size-exclusion analysis of radioactive compounds in tumours

The recovery of radioactivity from tumour homogenates was 95.7±7.2%, and that from the PD-10 columns was 85.5±6.9%. A major proportion of the radioactivity was eluted in a macromolecular fraction (78.7±6.7%).

**Table 3** Blocking study of the biodistribution of $^{125}$I-IBB in FM3A-implanted mice pretargeted with POS

| Organ | Vehicle | IBB treatment |
|---|---|---|
| Blood | 0.36±0.18 | 0.48±0.10 |
| Liver | 5.26±0.61 | 2.58±0.69* |
| Heart | 0.76±0.09 | 0.38±0.08 |
| Lung | 1.09±0.25 | 0.48±0.12 |
| Kidney | 12.15±5.03 | 2.44±0.41** |
| Stomach | 0.82±0.48 | 0.25±0.04 |
| Intestine | 9.04±3.77 | 5.06±2.30 |
| Tumour | 1.95±0.63 | 0.90±0.18* |
| Muscle | 0.51±0.06 | 0.16±0.04*** |
| Tumour/blood ratio | 5.49±1.12 | 1.93±0.38**** |

Organ uptake values are means±SD ($n$=5) in units of percent injected dose per gram of tissue, except for the stomach (percent injected dose) and tumour/blood ratio

*$p$<0.005, **$p$<0.001, ***$p$<0.0005, ****$p$<0.0001 vs. vehicle group

### In vivo imaging

Figure 1a shows the accumulation of $^{123}$I-IBB in the POS-pretargeted tumour. The tumour was clearly visualized 6 h after $^{123}$I-IBB injection, and the calculated tumour-to-muscle ratio was 4.6±1.4. The image was comparable to that obtained 24 h after $^{123}$I-IPOS injection, using the direct-targeting method (Fig. 1b; tumour-to-muscle ratio 6.9±1.6). Compared to the direct targeting method, with the pretargeting method, radioactivity decreased in the liver, but increased in the intestine. These findings were consistent with the biodistribution study data.

### $^{125}$I-IBB accumulation vs. HIF-1 transcriptional activity in tumours in mice pretargeted with POS

Figure 2 shows a positive correlation between HIF-1-induced luciferase bioluminescence and $^{125}$I-IBB accumulation 6 h after injection in tumours in mice pretargeted with POS ($R$=0.84, $p$<0.01).

### Regional distribution of $^{125}$I-IBB in the POS-pretargeted tumour

Dual fluorescent immunohistochemistry revealed the presence of HIF-1α- and PIMO-positive hypoxic areas in the tumour (Fig. 3a, b). The sections derived from PIMO-untreated mice were not stained with anti-PIMO antibody, and the HIF-1α signal was not detected in the negative control antibody-treated sections (data not shown). The autoradiogram showed that the distribution of $^{125}$I-IBB in the tumour was heterogeneous (Fig. 3c) and, for the most part, corresponded to the HIF-1α- and PIMO-positive hypoxic areas. However, there were also a few regions where the signal for HIF-1α or PIMO was positive, but where $^{125}$I-IBB had not accumulated (Fig. 3d, e). High-magnification merged imaging of HIF-1α and PIMO immunostaining revealed that HIF-1α-positive regions and

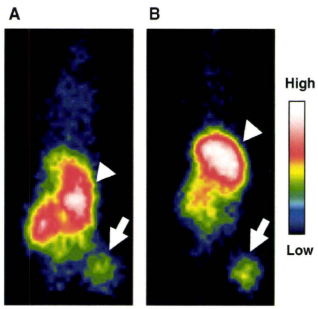


**Fig. 1** Typical planar images of FM3A-implanted mice acquired in the pretargeting method (**a**) and the direct-targeting method (**b**). Images were acquired 6 h after injection of $^{125}$I-IBB in the pretargeting method and 24 h after injection of $^{123}$I-IPOS in the direct targeting method. Tumours are clearly visualized (*arrows*) in a similar fashion in both images (*arrowheads* **a** intestine, **b** liver)

PIMO-positive regions were not always identical; some regions were positive for both, while other regions did not match (Fig. 3f). Therefore, we compared correlations between $^{125}$I-IBB accumulation and the expression of HIF-1α and PIMO. As shown in Fig. 4, significant positive correlations were found between the regional accumulation of $^{125}$I-IBB in POS-pretargeted tumour sections and the expression of both hypoxic markers (HIF-1α $R$=0.58, $p$<0.0001; PIMO $R$=0.34, $p$<0.005). The correlation coefficient between $^{125}$I-IBB and HIF-1α was greater than that with PIMO, although the difference was not statistically significant ($\chi^2$=3.13, $p$=0.077).

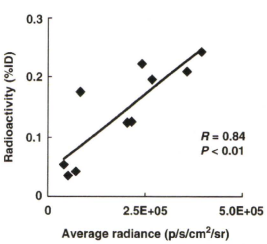


**Fig. 2** Correlation between $^{125}$I-IBB accumulation and HIF-1 transcriptional activity in the same tumour in mice pretargeted with POS. Mice carrying tumours with the HIF-1-dependent luciferase reporter gene in both thighs were used. The ordinate represents accumulated radioactivity (%ID), and the abscissa represents HIF-1-dependent luciferase bioluminescence. The correlation coefficient ($R$) was 0.84, indicating a highly significant correlation ($p$<0.01)

## Discussion

In the study reported here we showed rapid tumour imaging following pretargeting using POS and $^{123/125}$I-IBB. Using the pretargeting method, the tumoral accumulation (1.6% ID/g) and the tumour-to-blood ratio (4.2) 6 h after injection were found to be comparable to the data obtained 24 h after $^{125}$I-IPOS injection (1.4%ID/g, 5.1) [9]. The scintigraphic images of mice targeted with $^{123}$I-IPOS were very similar to those of prior studies, in which high signal levels were detected in the tumour, although the highest activity was seen in the liver even 24 h after injection [9]. In contrast, the images of the pretargeted mice clearly showed that $^{123}$I-IBB accumulated in the tumour more rapidly and cleared much more promptly from the body (with the exception of the intestine) than $^{123}$I-IPOS. These results indicate that the pretargeting method allows a shortening of the waiting time to one-fourth that required for direct targeting to obtain an adequate image. Clinical application of the pretargeting method in the future will contribute to a reduction in radiation exposure of the patient.

Recently it has been suggested that HIF-1 activates a number of genes, such as VEGF, erythropoietin, matrix metalloproteinase and glucose transporter, and that the expression level of HIF-1 correlates with a poor prognosis in many tumours [22–26]. Furthermore, the activation of such genes has an important role with respect to aggressive cancer phenotypes. Therefore, visualization and tumour therapy targeting for HIF-1 activation may be an important supplement to imaging of hypoxia per se when characterizing tumours. Some hypoxia imaging probes, including $^{18}$F-fluoromisonidazole ($^{18}$F-FMISO), 1-α-D-(5-deoxy-5-$^{18}$F-fluoroarabinofuranosyl)-2-nitroimidazole ($^{18}$F-FAZA) and $^{64}$Cu-diacetyl-bis($N^4$-methylthiosemicarbazone) ($^{64}$Cu-ATSM), have been developed [27]. They detect physically low oxygen pressure (<10 mmHg) and are useful in predicting the efficacy of radiotherapy [28]. However, the mechanisms underlying hypoxic accumulation of such probes are not dependent on HIF-1 expression [29]. Previously reported HIF-1-activity imaging systems required exogenous reporter gene transcription, which presents difficulties in practice [30, 31]. In contrast, our approach could assess HIF-1-activity directly, via a two-step targeting of the probes.

A recent immunohistochemical study has demonstrated the lack of complete colocalization between HIF-1α and PIMO. Sobhanifar et al. have reported that HIF-1 is expressed at higher levels of oxygen than those that allow PIMO metabolism and binding [32]. Thus, we compared the correlation between $^{125}$I-IBB accumulation and HIF-1α- and PIMO-positive regions. As shown in Fig. 4, the correlation coefficient between $^{125}$I-IBB and HIF-1α was greater than that between $^{125}$I-IBB and PIMO, although the

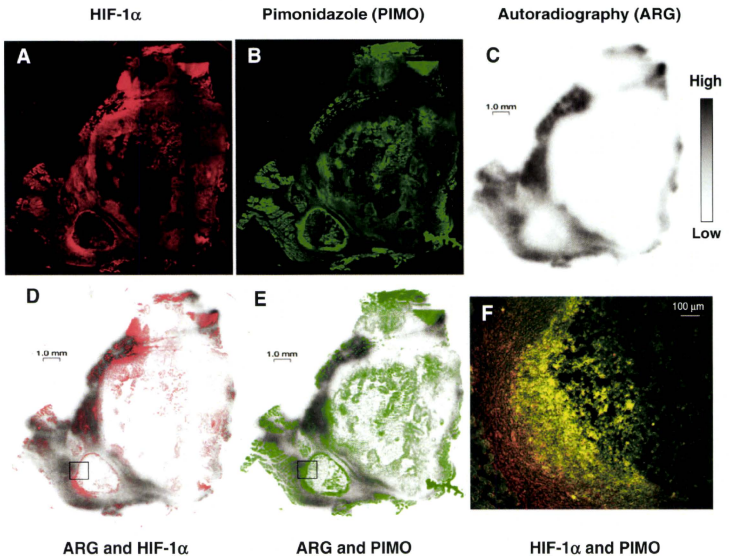


**Fig. 3** Comparison between the intratumoral distribution of $^{125}$I-IBB and the HIF-1α- and PIMO-positive hypoxic regions in POS-pretargeted tumours. **a**–**c** Typical images of HIF-1α immunostaining (**a**), PIMO immunostaining (**b**) and from autoradiography (**c**) in the same section. **d**, **e** Autoradiography image merged with HIF-1α immunostaining (**d**) and PIMO immunostaining (**e**) images. **f** High-magnification merged image of HIF-1α immunostaining and PIMO immunostaining (from insets in **d** and **e**). Some regions are both positive (*yellow*) and others do not match (*red* and *green*)

difference between the two correlation coefficients was not statistically significant. Therefore, the regions showing $^{125}$I-IBB accumulation potentially corresponded to the HIF-1α-positive regions and to the PIMO-positive regions but to a lesser degree. However, in the present study, the HIF-1α-positive region was mainly detected both in the PIMO-positive regions and in the surrounding regions (Fig. 3f). This result is consistent with those of a previous study, which showed that carbonic anhydrase 9, a HIF-1-regulated protein, generally colocates with PIMO though displaying greater extension in the direction of perfused areas [33]. Due to the overlap, the region showing $^{125}$I-IBB accumu-

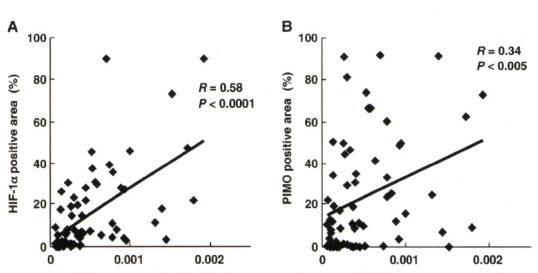


**Fig. 4** Correlation between areas showing $^{125}$I-IBB accumulation and HIF-1α- and PIMO-positive areas in POS-pretargeted tumours. A total of six sections (one section per tumour) were analysed. Quantitative analysis of autoradiograms provided data on $^{125}$I-IBB accumulation. $^{125}$I-IBB accumulation was positively correlated with HIF-1α and PIMO expression (HIF-1α $R$=0.58, $p$<0.0001; PIMO $R$=0.34, $p$<0.005)

lation also showed a weak positive correlation with the PIMO-positive regions. On the other hand, there were a few HIF-1α-negative regions in which $^{125}$I-IBB accumulated (Fig. 3d). This discrepancy could be explained by the delivery of POS and/or $^{125}$I-IBB. Since both probes were delivered by blood flow, they potentially tended to accumulate in regions rich in blood vessels, i.e. HIF-1α-negative regions. Because the degradation rate of POS was relatively slow [9], an excess of POS delivered to HIF-1α-negative regions could not be degraded, resulting in $^{125}$I-IBB accumulation in these regions. POS contains not only the essential domain related to the oxygen-dependent degradation of HIF-1α, but also PTD and SAV. These modifications may lower the rate of degradation, and this is a drawback of POS. However, it should be noted that by using the pretargeting method with POS and $^{123}$I-IBB, radioactivity accumulation was significantly correlated with the HIF-1α-positive region (Fig. 4a). Furthermore, accumulation of $^{123}$I-IBB was correlated with HIF-1 transcriptional activity in the tumours in mice pretargeted with POS (Fig. 2). Thus, our approach would detect not only hypoxic regions, but also HIF-1-active regions, and thus this approach could prove important to the qualitative diagnosis of and effective therapy against cancer.

In the pretargeting study, $^{125}$I-IBB accumulated in the tumours of POS-pretargeted mice. The accumulation was inhibited by nonradioactive IBB and D-biotin. Moreover, most of the radioactivity in the tumour existed as macromolecules. Taken together, the radioactivity in the tumour was caused by the binding of $^{125}$I-IBB to the SAV moiety of POS. Thus, $^{125}$I-IBB has the ability to bind to SAV, not only in vitro but also in vivo. It has been reported that the expression of HIF-1 is not ubiquitous, but heterogeneous, and is small in tumours [34]. Accumulation of the probe in tumours harbouring HIF-1-dependent reporter genes has been reported to be approximately 1%ID/g [34–36], which is comparable to the results of the present study.

In the biodistribution study of $^{125}$I-IBB alone, accumulation of radioactivity was highest in the intestine. This tissue distribution pattern reflects the behaviour of radioiodinated biotin itself, since $^{125}$I-IBB is not cleaved by serum biotinidase [17]. The high accumulation of $^{125}$I-IBB in the intestine resulted in high background activity in the abdominal region; therefore, the imaging of abdominal HIF-1-active tumours would be difficult. In this case, biotin derivatives that show faster clearance from the abdominal region than $^{125}$I-IBB are required. However, the background radioactivity in the thoracic region and cervicofacial region was generally low. The expression of HIF-1 has been reported to be associated with a poor prognosis in breast and lung cancers and in head and neck squamous cell carcinomas [26, 37, 38]; therefore, our imaging approach would be particularly useful for detecting HIF-1 activity in these tumours.

Recent studies have revealed that HIF-1 levels are controlled not only at the post-transcriptional level (that is, the oxygen-dependent regulation of the HIF-1α) but also at the transcriptional and translational levels [39, 40]. In a region where the transcription and translation of HIF-1α increases, an excess amount of HIF-1α is likely to saturate the ubiquitin/proteasome degradation system and result in the upregulation of HIF-1, even under mildly hypoxic conditions. This may be one reason why the threshold of oxygen pressure for HIF-1 stabilization varies and depends upon the character of the organs or tumours. In such regions, the POS degradation rate would also decrease, because it contains the ODD domain and degrades in the same manner as HIF-1α. Thus, in imaging with POS-pretargeting and $^{123}$I-IBB, it is possible to depict HIF-1-active regions that result from either hypoxic stabilization or the upregulation of transcription and translation.

## Conclusion

Using the pretargeting method, clear tumour images were obtained in a shorter time than was possible with the direct-labelling method. Intratumoral accumulations of $^{125}$I-IBB in the POS-pretargeted tumours were significantly correlated with HIF-1α-positive regions. These findings demonstrate that the pretargeting method with POS and $^{123}$I-IBB is effective for the rapid imaging of HIF-1-active tumour hypoxia.

**Acknowledgments** The authors would like to thank Nihon Medi-Physics for providing ammonium $^{123}$I-iodide. This work was supported in part by "R&D of Molecular Imaging Equipment for Malignant Tumor Therapy Support" of the New Energy and Industrial Technology Development Organization (NEDO), Japan, a Health Labour Sciences Research Grant for Research on Advanced Medical Technology from the Ministry of Health, Labour and Welfare of Japan, and a Grant-in-Aid for Exploratory Research (17659010) and a Grant-in-Aid for Young Scientists (B) (21791187) from the Ministry of Education, Culture, Sports, Science and Technology of Japan.

**Conflicts of interest** None.

## References

1. Vaupel P, Kallinowski F, Okunieff P. Blood flow, oxygen and nutrient supply, and metabolic microenvironment of human tumors: a review. Cancer Res 1989;49:6449–65.
2. Semenza GL. Expression of hypoxia-inducible factor 1: mechanisms and consequences. Biochem Pharmacol 2000;59:47–53.
3. Wenger RH. Cellular adaptation to hypoxia: O2-sensing protein hydroxylases, hypoxia-inducible transcription factors, and O2-regulated gene expression. FASEB J 2002;16:1151–62.
4. Ballinger JR. Imaging hypoxia in tumors. Semin Nucl Med 2001;31:321–9.
5. Kizaka-Kondoh S, Inoue M, Harada H, Hiraoka M. Tumor hypoxia: a target for selective cancer therapy. Cancer Sci 2003;94:1021–8.

6. Jiang BH, Semenza GL, Bauer C, Marti HH. Hypoxia-inducible factor 1 levels vary exponentially over a physiologically relevant range of O2 tension. Am J Physiol 1996;271:C1172–80.
7. Harada H, Kizaka-Kondoh S, Li G, Itasaka S, Shibuya K, Inoue M, et al. Significance of HIF-1-active cells in angiogenesis and radioresistance. Oncogene 2007;26:7508–16.
8. Harada H, Kizaka-Kondoh S, Hiraoka M. Optical imaging of tumor hypoxia and evaluation of efficacy of a hypoxia-targeting drug in living animals. Mol Imaging 2005;4:182–93.
9. Kudo T, Ueda M, Kuge Y, Mukai T, Tanaka S, Masutani M, et al. Imaging of HIF-1-active tumor hypoxia using a protein effectively delivered to and specifically stabilized in HIF-1-active tumor cells. J Nucl Med 2009;50:942–9.
10. Kizaka-Kondoh S, Konse-Nagasawa H. Significance of nitroimidazole compounds and hypoxia-inducible factor-1 for imaging tumor hypoxia. Cancer Sci 2009;100:1366–73.
11. Kizaka-Kondoh S, Tanaka S, Harada H, Hiraoka M. The HIF-1-active microenvironment: an environmental target for cancer therapy. Adv Drug Deliv Rev 2009;61:623–32.
12. Green NM. Avidin. 3. The nature of the biotin-binding site. Biochem J 1963;89:599–609.
13. Goldenberg DM, Rossi EA, Sharkey RM, McBride WJ, Chang CH. Multifunctional antibodies by the Dock-and-Lock method for improved cancer imaging and therapy by pretargeting. J Nucl Med 2008;49:158–63.
14. Sharkey RM, Cardillo TM, Rossi EA, Chang CH, Karacay H, McBride WJ, et al. Signal amplification in molecular imaging by pretargeting a multivalent, bispecific antibody. Nat Med 2005;11:1250–5.
15. Sharkey RM, Karacay H, Litwin S, Rossi EA, McBride WJ, Chang CH, et al. Improved therapeutic results by pretargeted radioimmunotherapy of non-Hodgkin's lymphoma with a new recombinant, trivalent, anti-CD20, bispecific antibody. Cancer Res 2008;68:5282–90.
16. Kizaka-Kondoh S, Itasaka S, Zeng L, Tanaka S, Zhao T, Takahashi Y, et al. Selective killing of hypoxia-inducible factor-1-active cells improves survival in a mouse model of invasive and metastatic pancreatic cancer. Clin Cancer Res 2009;15:3433–41.
17. Foulon CF, Alston KL, Zalutsky MR. Synthesis and preliminary biological evaluation of (3-iodobenzoyl)norbiotinamide and ((5-iodo-3-pyridinyl)carbonyl)norbiotinamide: two radioiodinated biotin conjugates with improved stability. Bioconjug Chem 1997;8:179–86.
18. Motta-Hennessy C, Sharkey RM, Goldenberg DM. Metabolism of indium-111-labeled murine monoclonal antibody in tumor and normal tissue of the athymic mouse. J Nucl Med 1990;31:1510–9.
19. Ishino S, Kuge Y, Takai N, Tamaki N, Strauss HW, Blankenberg FG, et al. 99mTc-Annexin A5 for noninvasive characterization of atherosclerotic lesions: imaging and histological studies in myocardial infarction-prone Watanabe heritable hyperlipidemic rabbits. Eur J Nucl Med Mol Imaging 2007;34:889–99.
20. Ishino S, Mukai T, Kuge Y, Kume N, Ogawa M, Takai N, et al. Targeting of lectinlike oxidized low-density lipoprotein receptor 1 (LOX-1) with 99mTc-labeled anti-LOX-1 antibody: potential agent for imaging of vulnerable plaque. J Nucl Med 2008;49:1677–85.
21. Ueda M, Iida Y, Tominaga A, Yoneyama T, Ogawa M, Magata Y, et al. Nicotinic acetylcholine receptors expressed in the ventral posterolateral thalamic nucleus play an important role in anti-allodynic effects. Br J Pharmacol 2010;159:1201–10.
22. Harada H, Xie X, Itasaka S, Zeng L, Zhu Y, Morinibu A, et al. Diameter of tumor blood vessels is a good parameter to estimate HIF-1-active regions in solid tumors. Biochem Biophys Res Commun 2008;373:533–8.
23. Marignol L, Coffey M, Lawler M, Hollywood D. Hypoxia in prostate cancer: a powerful shield against tumour destruction? Cancer Treat Rev 2008;34:313–27.
24. Ke HL, Wei YC, Yang SF, Li CC, Wu DC, Huang CH, et al. Overexpression of hypoxia-inducible factor-1alpha predicts an unfavorable outcome in urothelial carcinoma of the upper urinary tract. Int J Urol 2008;15:200–5.
25. Miyake K, Yoshizumi T, Imura S, Sugimoto K, Batmunkh E, Kanemura H, et al. Expression of hypoxia-inducible factor-1alpha, histone deacetylase 1, and metastasis-associated protein 1 in pancreatic carcinoma: correlation with poor prognosis with possible regulation. Pancreas 2008;36:e1–9.
26. Trastour C, Benizri E, Ettore F, Ramaioli A, Chamorey E, Pouyssegur J, et al. HIF-1alpha and CA IX staining in invasive breast carcinomas: prognosis and treatment outcome. Int J Cancer 2007;120:1451–8.
27. Mees G, Dierckx R, Vangestel C, Van de Wiele C. Molecular imaging of hypoxia with radiolabelled agents. Eur J Nucl Med Mol Imaging 2009;36:1674–86.
28. Dunphy MP, Lewis JS. Radiopharmaceuticals in preclinical and clinical development for monitoring of therapy with PET. J Nucl Med 2009;50 Suppl 1:106S–21S.
29. Krohn KA, Link JM, Mason RP. Molecular imaging of hypoxia. J Nucl Med 2008;49 Suppl 2:129S–48S.
30. He F, Deng X, Wen B, Liu Y, Sun X, Xing L, et al. Noninvasive molecular imaging of hypoxia in human xenografts: comparing hypoxia-induced gene expression with endogenous and exogenous hypoxia markers. Cancer Res 2008;68:8597–606.
31. Yeom CJ, Chung JK, Kang JH, Jeon YH, Kim KI, Jin YN, et al. Visualization of hypoxia-inducible factor-1 transcriptional activation in C6 glioma using luciferase and sodium iodide symporter genes. J Nucl Med 2008;49:1489–97.
32. Sobhanifar S, Aquino-Parsons C, Stanbridge EJ, Olive P. Reduced expression of hypoxia-inducible factor-1alpha in perinecrotic regions of solid tumors. Cancer Res 2005;65:7259–66.
33. Li XF, Carlin S, Urano M, Russell J, Ling CC, O'Donoghue JA. Visualization of hypoxia in microscopic tumors by immunofluorescent microscopy. Cancer Res 2007;67:7646–53.
34. Serganova I, Doubrovin M, Vider J, Ponomarev V, Soghomonyan S, Beresten T, et al. Molecular imaging of temporal dynamics and spatial heterogeneity of hypoxia-inducible factor-1 signal transduction activity in tumors in living mice. Cancer Res 2004;64:6101–8.
35. Hsieh CH, Kuo JW, Lee YJ, Chang CW, Gelovani JG, Liu RS. Construction of mutant TKGFP for real-time imaging of temporal dynamics of HIF-1 signal transduction activity mediated by hypoxia and reoxygenation in tumors in living mice. J Nucl Med 2009;50:2049–57.
36. Wen B, Burgman P, Zanzonico P, O'Donoghue J, Cai S, Finn R, et al. A preclinical model for noninvasive imaging of hypoxia-induced gene expression; comparison with an exogenous marker of tumor hypoxia. Eur J Nucl Med Mol Imaging 2004;31:1530–8.
37. Ioannou M, Papamichali R, Kouvaras E, Mylonis I, Vageli D, Kerenidou T, et al. Hypoxia inducible factor-1 alpha and vascular endothelial growth factor in biopsies of small cell lung carcinoma. Lung 2009;187:321–9.
38. van den Broek GB, Wildeman M, Rasch CR, Armstrong N, Schuuring E, Begg AC, et al. Molecular markers predict outcome in squamous cell carcinoma of the head and neck after concomitant cisplatin-based chemoradiation. Int J Cancer 2009;124:2643–50.
39. North S, Moenner M, Bikfalvi A. Recent developments in the regulation of the angiogenic switch by cellular stress factors in tumors. Cancer Lett 2005;218:1–14.
40. Skinner HD, Zheng JZ, Fang J, Agani F, Jiang BH. Vascular endothelial growth factor transcriptional activation is mediated by hypoxia-inducible factor 1alpha, HDM2, and p70S6K1 in response to phosphatidylinositol 3-kinase/AKT signaling. J Biol Chem 2004;279:45643–51.

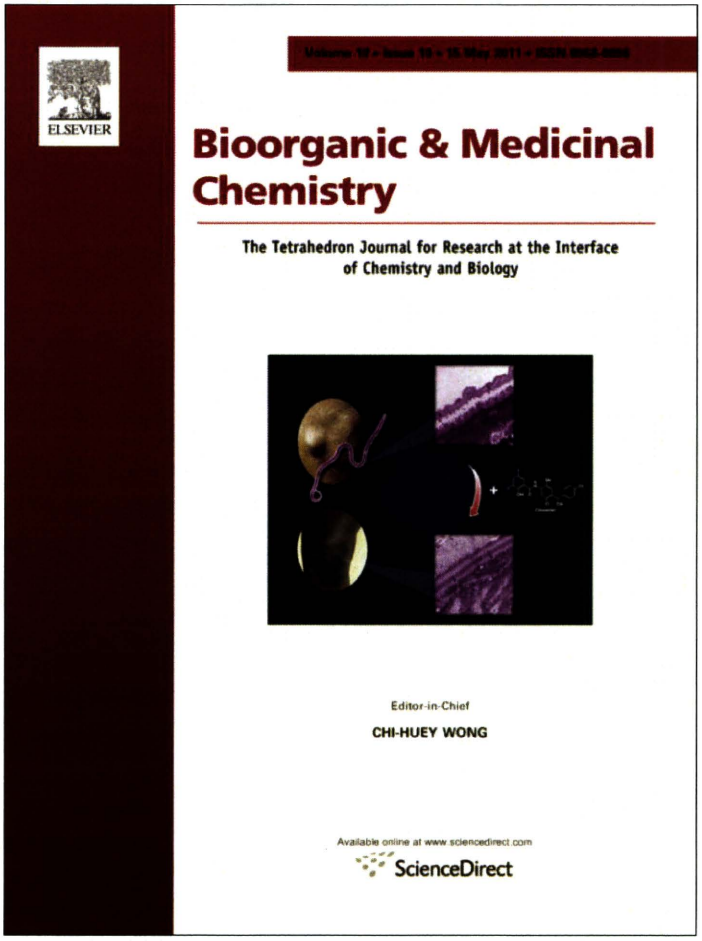

Bioorganic & Medicinal Chemistry 19 (2011) 3216–3220

Contents lists available at ScienceDirect

Bioorganic & Medicinal Chemistry

journal homepage: www.elsevier.com/locate/bmc

# Concise site-specific synthesis of DTPA–peptide conjugates: Application to imaging probes for the chemokine receptor CXCR4

Ryo Masuda, Shinya Oishi *, Hiroaki Ohno, Hiroyuki Kimura, Hideo Saji, Nobutaka Fujii *

*Graduate School of Pharmaceutical Sciences, Kyoto University, Sakyo-ku, Kyoto 606-8501, Japan*

ARTICLE INFO

*Article history:*
Received 17 February 2011
Revised 25 March 2011
Accepted 26 March 2011
Available online 2 April 2011

*Keywords:*
CXCR4
DTPA
Molecular imaging

ABSTRACT

Diethylenetriaminepentaacetic acid (DTPA) is a useful chelating agent for radionuclides such as $^{68}$Ga, $^{99m}$Tc and $^{111}$In, which are applicable to nuclear medicine imaging. In this study, we established a facile synthetic protocol for the production of mono-DTPA-conjugated peptide probes. A novel monoreactive DTPA precursor reagent was synthesized in two steps using the chemistry of the *o*-nitrobenzenesulfonyl (Ns) protecting group, and under mild conditions this DTPA precursor was incorporated onto an $N^{\varepsilon}$-bromoacetylated Lys of a protected peptide resin. The site-specific DTPA conjugation was facilitated by using a highly acid-labile 4-methyltrityl (Mtt) protecting group for the target site of the bioactive peptide during the solid-phase synthesis. A combination of both techniques yielded peptides with disulfide bonds, such as octreotide and polyphemusin II-derived CXCR4 antagonists. DTPA–peptide conjugates were purified in a single step following cleavage from the resin and disulfide bond formation. This site-specific on-resin construction strategy was used for the design and synthesis of a novel In-DTPA-labeled CXCR4 antagonist, which exhibited highly potent inhibitory activity against SDF-1–CXCR4 binding.



## 1. Introduction

Recent progress in molecular imaging methodologies such as positron emission tomography (PET), single-photon emission computed tomography (SPECT) and optical imaging technologies has significantly improved the early detection and diagnosis of malignant tumors. To visualize the specific molecular events involved in the physiological and/or pathological processes, a number of peptide-based imaging probes have been developed for overexpressed receptors of peptide hormones and extracellular matrix proteins.[1] These probes are usually designed by a combination of three components: a target-specific vector peptide, an imaging part such as a radionuclide or fluorophore, and a linker to covalently or noncovalently conjugate the peptide with the imaging moiety. The addition of a functional moiety onto small-sized bioactive peptides may be highly susceptible to interaction with receptors or counterpart molecules. Consequently, there have been many reagents of choice for appropriate protein/peptide modifications. In addition, to determine the best labeling position from structure-function relationship studies, versatile synthetic approaches toward various types of labeled peptide are desired.

Polyamino polycarboxylate ligands efficiently coordinate metal radioisotopes to aid the radiolabeling of bioactive peptides. Among the chelating ligands, 1,4,7,10-tetraazacyclododecane-1,4,7,10-tetraacetic acid (DOTA) **1a** has been most widely utilized, since a variety of metal radioisotopes for both diagnostic and therapeutic purposes form complexes with high affinity and kinetic stability (Fig. 1).[2] DOTA-modification of bioactive peptides is facilitated by commercially available reagents such as DOTA-NHS **1b** and DOTA-maleimide **1c** to provide the expected peptides in a single step.[3,4] Alternatively, tris(*tert*-butyl)-DOTA **2a** with a free carboxyl group is employed for the modification of an amino group of protected peptides bound to solid-supports.[5] Lysine or phenylalanine derivatives **2b,c** possessing a *tert*-butyl-protected DOTA moiety are also useful components for the peptide sequence assembly.[6] *tert*-Butyl protecting groups in these reagents are easily removed during the final side-chain deprotection process of peptide synthesis.

In contrast to these DOTA derivatives, there has been limited work exploring the application of the diethylenetriaminepentaacetic acid (DTPA) chelating group **3a**, although DTPA represents a promising alternative, especially for $^{68}$Ga, $^{99m}$Tc and $^{111}$In (Fig. 1). The recent success of DTPA-based probes is exemplified by a glucagon-like peptide-1 (GLP-1) receptor ligand, [Lys$^{40}$(Ahx-DTPA-$^{111}$In)$NH_2$]-exendin-4, for insulinoma diagnosis.[7] The DTPA group also works as a more favorable functional group than DOTA to facilitate the biological or biodistribution properties of several probes.[8] For the preparation of DTPA-conjugated imaging probes, several conjugation reagents have been developed. The most familiar cyclic diethylenetriaminepentaacetic dianhydride **4**

* Corresponding authors. Tel.: +81 75 753 4551; fax: +81 75 753 4570.
*E-mail addresses:* soishi@pharm.kyoto-u.ac.jp (S. Oishi), nfujii@pharm.kyoto-u.ac.jp (N. Fujii).

0968-0896/$ - see front matter © 2011 Elsevier Ltd. All rights reserved.
doi:10.1016/j.bmc.2011.03.059

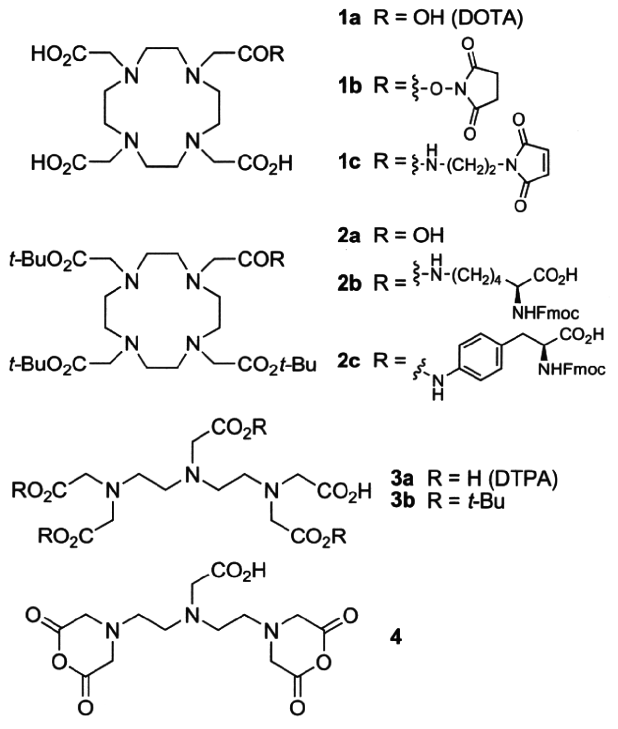


**Figure 1.** Structures of radionuclide chelating agents and the precursors.

is a bifunctional chelating agent, which can conjugate with peptide hormones and antibodies.[9] Using this reagent, concomitant formations of a bis-conjugated product[10] and intra- and intermolecular cross-linked products[11] were unavoidable. Monoreactive DTPA derivatives have also been developed for the preparation of DTPA–peptide conjugates without the unfavorable by-product formations.[12,13] For example, we reported the synthesis and application of 3,6,9,9-tetrakis[(*tert*-butoxycarbonyl)methyl]-3,6,9-triazanonanoic acid **3b** (mDTPA),[14] in which the four carboxylates were protected with *tert*-butyl ester. However, a longer process from the commercially available reagents is required for the synthesis of these DTPA-conjugation reagents (Scheme 1A).

Accordingly, to establish a facile and efficient synthetic method for DTPA–peptide conjugates, we have investigated the site-specific and on-resin construction of a DTPA moiety. Herein, we describe the short-step synthesis of a DTPA precursor using the *o*-nitrobenzenesulfonyl (Ns) protecting group and the solid-phase synthesis of DTPA–peptide conjugates. The design and synthesis of DTPA–peptide conjugates that potentially target the somatostatin receptor and chemokine receptor CXCR4 are also presented.[15]

## 2. Results and discussion

### 2.1. Synthesis of a DTPA-conjugation reagent and the application to octreotide derivatives

The synthetic scheme for the production of mDTPA reagent **10**, as described in our previous study, is presented in Scheme 1A. We hypothesized that two remedies could significantly improve the overall synthetic process of DTPA–peptide conjugates. First, the use of an Ns group in place of the trifluoroacetyl group was expected to serve as a temporary protecting group and an auxiliary group for global modification with four *tert*-butoxycarbonylmethyl groups. This potentially improves the stepwise synthesis of the intermediate **7** in the solution-phase. In addition, a secondary amine **8** as a nucleophilic precursor for the bromoacetyl group on peptide resin **11** can directly produce the overall DTPA framework of **12** on the solid support without the additional three-step modification process of **8** in solution (Scheme 1B).[16]

Synthesis of DTPA precursor **8** began with mono-Ns protection of the commercially available diethylenetriamine **5** (Scheme 2). The Ns-protected intermediate was successively treated with excess equivalent of *t*-butyl bromoacetate in a one-pot process. Although the solvent EtOH has been reported to be effective in predominantly giving the mono-Ns product,[17] concomitant production of bis-Ns product **14b** was not suppressed as in DMF. The treatment of excess diethylenetriamine **5** with NsCl in EtOH provided mono-Ns product **14a** in 65% yield (calculated based on NsCl), which can be readily purified by chromatography. Compound **14a** was then subjected to deprotection with mercaptoacetic acid and LiOH to provide the expected precursor **8** in 77% yield.

Using the resulting reagent **8**, DTPA-conjugation of [D-Phe$^1$]octreotide was investigated as a model study (Scheme 3), which is employed as a radionuclide imaging probe for the somatostatin receptor.[14,18,19] After peptide-chain elongation by Fmoc-based solid-phase peptide synthesis, the N-terminus of **16** was modified with bromoacetic acid and 1,3-diisopropylcarbodiimide (DIC). Subsequently, the bromide **17** was treated with the reagent **8** in the presence of $(i\text{-Pr})_2$NEt to provide the fully protected peptide resin **18a**. Cleavage from the resin **18a** and disulfide formation under air-oxidation conditions provided [DTPA-D-Phe$^1$]octreotide **19a** with high purity. The bromoacetylated peptide **17** was also modified with commercially available DOTA precursor reagent **20**, using the identical procedure to provide [DOTA-D-Phe$^1$]octreotide **19b**.[20] These suggest that this on-resin modification procedure is widely applicable to any chelating reagents with nucleophilic functional groups such as DTPA and DOTA precursors.

### 2.2. Site-specific DTPA-conjugation of bioactive peptides: synthesis of CXCR4 receptor probes

It has been reported that a high level of CXCR4 expression in tumors is associated with malignant and metastatic properties.[21] Intrinsic SDF-1 release from the potential distal metastatic sites mediates organ-specific metastasis of CXCR4-expressing cells from the primary lesions. Since CXCR4-expressing cancer stem cells are related to the metastatic spread in orthotopic primary tumors,[22] it is of considerable importance to develop potent CXCR4-imaging probes to detect potential cancer stem cells within malignant tumors, as exemplified by the diagnosis of bladder cancer by a fluorescent CXCR4 probe.[23,24]

Previously, we reported a DTPA-conjugated CXCR4 antagonist, DTPA-Ac-TZ14011 **26a**,[25] which was designed from a horseshoe crab-derived anti-HIV peptide T140. This peptide has β-sheet-like structures maintained by a disulfide bond, around which the pharmacophore residues for bioactivity are located.[26] For the site-specific conjugation at D-Lys$^8$ in the type II' β-turn region of T140 with a single DTPA group in the solution-phase, a secondary lysine (Lys$^7$) was substituted with arginine, which cannot be acylated by standard reagents.[25] Although a DTPA group was successfully ligated with maintenance of highly potent CXCR4 antagonistic activity in this case,[25] the accompanying substitutions needed for specific modification of other peptides may possibly lead to a decrease in the bioactivity. Therefore, we planned the facile site-specific DTPA conjugation on a solid-support for production of CXCR4 imaging probes without substitution of the secondary Lys$^7$ residue. To distinguish D-Lys$^8$ to be labeled in peptides **26**, the highly acid-labile 4-methyltrityl (Mtt) group was exploited for temporary protection of the ε-amino group during solid-phase peptide synthesis.[27] For the other Lys residues such as Lys$^7$ of

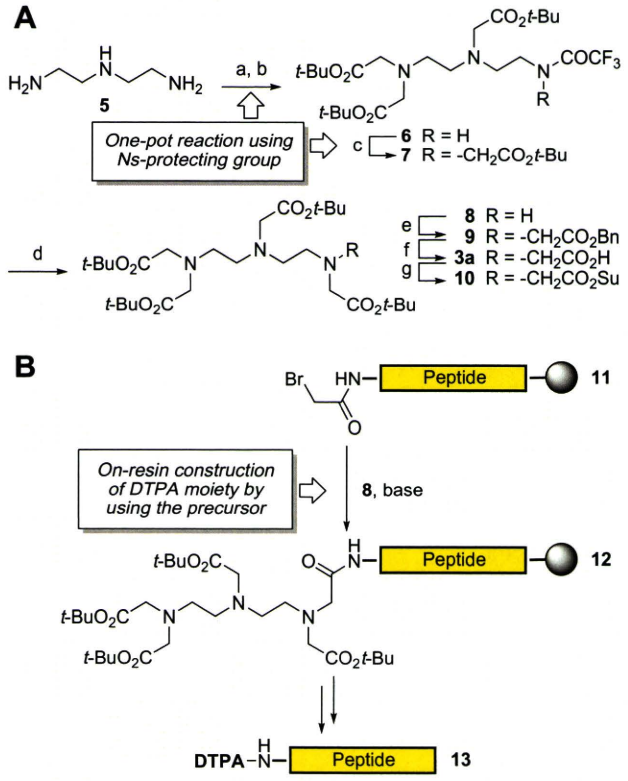


**Scheme 1.** (A) Synthetic scheme for the DTPA-conjugation reagent **10** prepared in our previous study; (B) synthetic plan for the DTPA-conjugated peptides in this study. Reagents: (a) $CF_3CO_2Et$; (b) $BrCH_2CO_2t$-Bu, $(i\text{-}Pr)_2NEt$; (c) $BrCH_2CO_2t$-Bu, NaH; (d) $NH_2NH_2$, $t$-BuOH; (e) $BrCH_2CO_2Bn$, $(i\text{-}Pr)_2NEt$; (f) $H_2$, Pd/C; (g) DCC, HOSu.

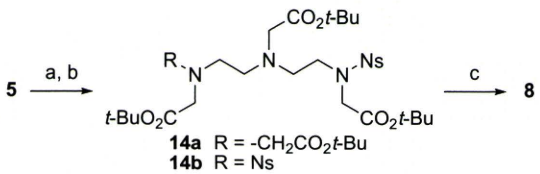


**Scheme 2.** Synthesis of DTPA precursor **8** via a global N-alkylation process using a Ns-protecting group. Reagents: (a) NsCl; (b) $BrCH_2CO_2t$-Bu, $K_2CO_3$; (c) $HSCH_2CO_2H$, LiOH.

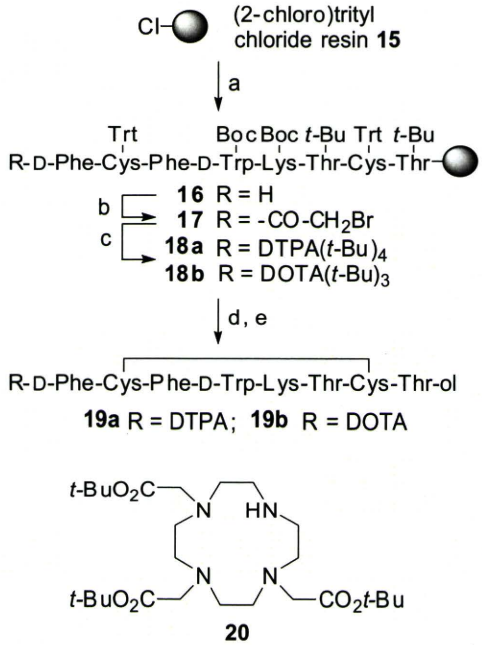


**Scheme 3.** Synthesis of DTPA- and DOTA-conjugated D-Phe-octreotides. Reagents: (a) Fmoc-based peptide synthesis; (b) $BrCH_2CO_2H$, DIC; (c) **8** for **18a**, or **20** for **18b**, $(i\text{-}Pr)_2NEt$ (d) TFA/$H_2O$/1,2-ethanedithiol (EDT) (95:2.5:2.5) for **19a**, 1 M TMSBr, thioanisole/TFA, 1,2-ethanedithiol, *m*-cresol for **19b**; (e) $NH_4OH$ (air oxidation).

**26b,c**, a Boc group was employed. This group can be cleaved by the standard TFA-based treatment in Fmoc chemistry (Scheme 4). After the construction of the protected peptide resin, the orthogonal Mtt group at the labeling position was cleaved off using 1,1,1,3,3,3-hexafluoropropan-2-ol (HFIP). The resulting ε-amino group was successively modified with bromoacetic acid followed by the reagent **8** to provide the fully protected DTPA–peptide resin **25**. Final deprotection, air-oxidation and HPLC purification afforded the expected DTPA-conjugated CXCR4 antagonists **26a,b**. This concise protocol facilitates the selection of chelating structure and position(s) on the peptide chain, and aids structure–activity relationship studies aimed at exploring the more potent peptide probes. For example, a 4-fluorobenzoyl modification at the N-terminus, which should increase CXCR4 antagonism,[28] was easily appended to the peptide using this protocol to give the modified peptide **26c**. The subsequent treatment with nonradioactive $InCl_3$ in acidic conditions provided the In-DTPA-labeled CXCR4 antagonists **27a–c**.

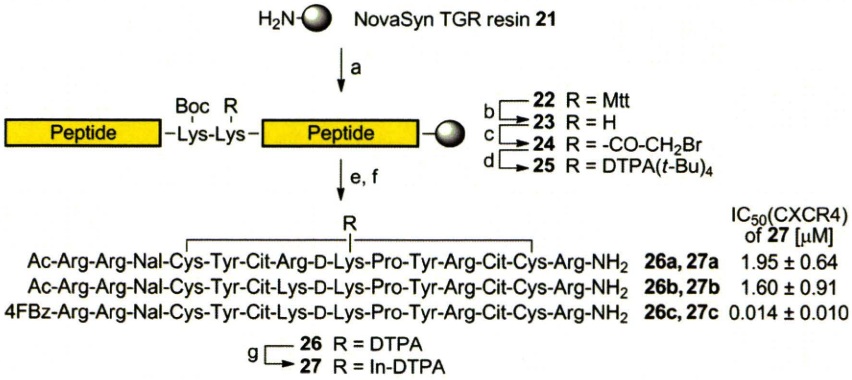


**Scheme 4.** Site-specific In-DTPA labeling of CXCR4 antagonists and biological activity. Reagents: (a) Fmoc-based peptide synthesis; (b) $CH_2Cl_2$/1,1,1,3,3,3-hexafluoro-2-propanol (HFIP)/2,2,2-trifluoroethanol (TFE)/triethylsilane (TES) (65:20:10:5); (c) $BrCH_2CO_2H$, DIC; (d) **8**, $(i\text{-}Pr)_2NEt$; (e) TFA/$H_2O$/EDT (95:2.5:2.5); (f) $NH_4OH$ (air oxidation); (g) $InCl_3$. *Abbreviations:* Mtt: 4-methyltrityl; Cit: L-citrulline, Nal: L-3-(2-naphthyl)alanine, 4FBz: 4-fluorobenzoyl.

### 2.3. Bioactivity of In-DTPA-labeled CXCR4 antagonists

The biological activity of the In-DTPA-labeled peptides **27a–c** was evaluated as the inhibitory potency of [$^{125}$I]-SDF-1-binding to CXCR4 membrane extracts (Scheme 4). Peptides **27a,b**, with an N-terminal acetyl group, exhibited similar potency towards CXCR4 [$IC_{50}$(**27a**) = 1.95 ± 0.64 μM, $IC_{50}$(**27b**) = 1.60 ± 0.91 μM], indicating that the Lys and Arg for the *i*-position of β-turn were both tolerant to the bioactivity. In contrast, peptide **27c** exerted much more potent inhibitory activity for the SDF-1 binding to CXCR4 [$IC_{50}$(**27c**) = 0.014 ± 0.010 μM]. These results of In-DTPA-labeled peptides **27a–c** coincided with our previous report on the unlabeled peptides.[28] The novel potent In-DTPA-labeled CXCR4 antagonist **27c** could be a promising imaging probe for CXCR4-expressing malignant cancer cells.[11]

## 3. Conclusions

In this study, we have established a novel synthetic method for the production of DTPA–peptide conjugates. The process includes facile solid-phase synthesis of a DTPA framework using a novel precursor substrate and site-specific conjugation using a highly acid-labile protecting group. Using a temporary Ns protecting group, the DTPA precursor **8** was obtained through two purification steps from commercially available diethylenetriamine. In addition, the on-resin incorporation of a bromoacetyl group into the specific free amino group followed by the addition of the nucleophilic DTPA precursors provided the expected DTPA–peptide conjugates with high purity. Taking advantage of secondary amine precursors of choice, these processes represent versatile methods to prepare a series of peptide conjugates, including DTPA and DOTA, for optimization of imaging probes. This conjugation method was applied to the preparation of DTPA-conjugates of octreotide and CXCR4 antagonist, which have been reported to effectively detect cancer cells. The peptide **27c** with highly potent inhibitory activity of SDF-1 binding to CXCR4 was obtained without any amino acid substitution to avoid multiple modifications on the amino groups. This peptide represents a promising lead compound as an imaging probe towards CXCR4-positive metastatic tumors.

## 4. Experimental

### 4.1. Synthesis

#### 4.1.1. Bis(*tert*-butyl) 3,6-bis[(*tert*-butoxycarbonyl)methyl]-9-(*o*-nitrobenzenesulfonyl)-3,6,9-triazaundecanedioate (14a)

To diethylenetriamine **5** (0.540 mL, 5.00 mmol) in dehydrated EtOH (5 mL), *o*-NsCl (0.367 g, 1.67 mmol) was slowly added below 0 °C. After stirring for 2 h, EtOH was removed in vacuo. To dehydrated DMF (8 mL), $K_2CO_3$ (4.49 g, 32.5 mmol) and $BrCH_2CO_2t$-Bu (4.06 mL, 27.5 mmol) were added at 0 °C. The mixture was stirred overnight at room temperature, and filtered. The filtrate was concentrated under reduced pressure to give an oily residue, and the residue was dissolved in EtOAc (100 mL). The whole mixture was washed with saturated $NaHCO_3$, and was dried over $MgSO_4$. Concentration under reduced pressure followed by flash chromatography over silica gel with *n*-hexane–EtOAc gave compound **14a** as a yellow oil (0.81 g, 65%); $^1$H NMR ($CDCl_3$, 500 MHz) δ 8.08–8.11 (1H, m), 7.64–7.69 (2H, m), 7.56–7.60 (1H, m), 4.24 (2H, s), 3.49 (2H, t, *J* = 6.9 Hz), 3.42 (4H, s), 3.30 (2H, s), 2.88 (2H, t, *J* = 6.6 Hz), 2.78 (2H, t, *J* = 6.9 Hz), 2.77 (2H, t, *J* = 6.9 Hz), 1.45 (27H, s), 1.36 (9H, s); $^{13}$C NMR ($CDCl_3$, 500 MHz) δ 170.6 (3C), 168.0, 133.7, 133.2, 131.6 (2C), 130.9, 123.9, 82.0, 81.0, 80.9 (2C), 56.1 (3C), 53.3, 52.8, 52.4, 49.4, 46.7, 28.1 (9C), 27.9 (3C); HRMS (FAB) *m*/*z* calcd for $C_{34}H_{58}N_4O_{12}S$ ([M+H]$^+$): 746.3772, found 746.3779.

#### 4.1.2. Bis(*tert*-butyl) 3,6-bis[(*tert*-butoxycarbonyl)methyl]-3,6,9-triazaundecanedioate (8)

To a solution of compound **14a** (0.216 g, 0.29 mmol) in DMF (0.726 mL), LiOH (0.128 g, 2.90 mmol) and mercaptoacetic acid (0.101 mL, 1.45 mmol) were added below 0 °C. After stirring for 2 h at room temperature, the mixture was concentrated under reduced pressure, and the residue was dissolved in $CHCl_3$. The whole reaction mixture was washed with saturated $NaHCO_3$, and was dried over $Na_2SO_4$. Concentration under reduced pressure followed by flash chromatography over silica gel with $CHCl_3$–MeOH gave compound **8** as a yellow oil (0.124 g, 77%); $^1$H NMR ($CDCl_3$, 500 MHz) δ 3.39 (4H, s), 3.28 (4H, s), 2.72–2.82 (6H, m), 2.63 (2H, t, *J* = 5.4 Hz), 1.39 (9H, s), 1.38 (27H, s); $^{13}$C NMR ($CDCl_3$, 500 MHz) δ 170.9, 170.7 (3C), 80.8 (4C), 55.9 (2C), 55.8 (2C), 52.4, 52.3, 51.3, 47.0, 28.2 (3C), 28.1 (9C); HRMS (FAB) *m*/*z* calcd for $C_{28}H_{54}N_3O_8$ ([M+H]$^+$): 560.3911, found 560.3910.

#### 4.1.3. Standard procedure for solid-phase peptide synthesis

Protected peptide-resins were manually constructed by Fmoc-based solid-phase peptide synthesis. *t*-Bu ester for Asp and Glu; 2,2,4,6,7-pentamethyldihydrobenzofurane-5-sulfonyl (Pbf) for Arg; *t*-Bu for Thr and Tyr; Boc for Lys and Trp; Trt for Cys were employed for side-chain protection. Fmoc-amino acids were coupled using three equivalents of reagents [Fmoc-amino acid, 1,3-diisopropylcarbodiimide (DIC), and HOBt·$H_2O$] to the free amino group in DMF for 1.5 h. Fmoc deprotection was performed by 20% (v/v) piperidine in DMF (2 × 1 min, 1 × 30 min). The protected peptide resin was treated with a cocktail of deprotection reagents. After removal of the resin by filtration, the filtrate was poured into ice-cold dry $Et_2O$. The resulting powder was collected by centrifugation and washed with ice-cold dry $Et_2O$. The crude peptide was dissolved in $H_2O$, and the pH was adjusted to 8.0 with $NH_4OH$ for disulfide bond formation. After air-oxidation for 1 d, the crude product was purified by preparative HPLC on a Cosmosil 5C18-ARII preparative column (Nacalai Tesque, Kyoto, Japan; 20 × 250 mm, flow rate 10 mL/min) to afford the expected peptides. All peptides were characterized by MALDI-TOF-MS (AXIMA-CFR plus, Shimadzu, Kyoto, Japan) and the purity was calculated as >95% by HPLC on a Cosmosil 5C18-ARII analytical column (Nacalai Tesque, 4.6 × 250 mm, flow rate 1 mL/min) at 220 nm absorbance.

#### 4.1.4. Preparation of DTPA- and DOTA-conjugated octreotides (19a,b)

According to the procedure reported previously,[18] (2-chloro)trityl chloride resin **15** (214 mg, 1.4 mmol/g), Fmoc-Thr(*t*-Bu)-ol (345 mg, 0.9 mmol), and pyridine (0.145 mL, 1.8 mmol) were agitated for 21 h in dry $CH_2Cl_2$–DMF (1:1, 3.94 mL). The loading was determined by measuring the 290 nm UV absorption of the piperidine-treated sample (0.455 mmol/g). After the construction of the peptide chain (0.017 mmol scale) using a standard procedure, bromoacetic acid (23.6 mg, 0.17 mmol) with DIC (0.026 mL, 0.17 mmol) in $CH_2Cl_2$ was reacted with resin **16** for 2 h at room temperature. The subsequent treatment of **17** with amines **8** (29.0 mg, 0.51 mmol) and **20** (26.3 mg, 0.51 mmol) with (*i*-Pr)$_2$NEt (0.009 mL, 0.51 mmol) in DMF for 12 h at room temperature provided **18a** and **18b**, respectively. Cleavage and deprotection of **18a** (72.5 mg) and **18b** (73.8 mg) was achieved using a TFA/1,2-ethandithiol (EDT)/$H_2O$ (5 mL; 95:2.5:2.5) cocktail for 2 h at room temperature and by treatment with 1 M TMSBr-thioanisole/TFA in the presence of EDT/*m*-cresol (3.3 mL) for 2 h at 0 °C, respectively. After disulfide formation under air-oxidation conditions, the crude peptides were purified using the standard procedure, to afford the desired peptides **19a** (8.2 mg, 23%) and **19b** (9.5 mg, 26%) as white powders. Compound **19a**: MS (MALDI-TOF) *m*/*z* calcd for $C_{63}H_{89}N_{13}O_{19}S_2$ ([M+H]$^+$): 1395.6, found 1395.3. Compound **19b**:

MS (MALDI-TOF) *m/z* calcd for $C_{65}H_{93}N_{14}O_{17}S_2$ ([M+H]$^+$): 1405.6, found 1405.8.

#### 4.1.5. Preparation of DTPA-conjugated CXCR4 antagonists (26a–c)

Protected peptide resins were manually constructed according to the standard procedure using NovaSyn TGR-resin **21** (96.2 mg, 0.025 mmol). 4-Methyltrityl (Mtt) group was employed for the protection of the D-Lys ε-amino group. The N-terminal amino group was acylated by treatment with $Ac_2O$ (0.012 mL, 0.125 mmol)/pyridine (0.020 mL, 0.250 mmol) for 1 h at room temperature for peptides **26a,b**, and with 4-fluorobenzoic acid (17.5 mg, 0.125 mmol)/DIC (0.019 mL, 0.125 mmol)/HOBt·$H_2O$ (19.2 mg, 0.125 mmol) for 1.5 h at room temperature for peptide **26c**. Subsequently, the resin **22** was treated with $CH_2Cl_2$/1,1,1,3,3,3-hexafluoropropan-2-ol (HFIP)/trifluoroethanol (TFE)/triethylsilane (TES) [65:20:10:5; 5 mL] for 2 h at room temperature. The DTPA group was incorporated using the identical procedure employed for the synthesis of the octreotide derivative **19a**. Treatment of the resins (**25a**: 178 mg, **25b**: 165 mg, **25c**: 162 mg) with a TFA/1,2-ethandithiol(EDT)/$H_2O$ (95:2.5:2.5; 5 mL) cocktail for 2 h at room temperature followed by air oxidation and purification provided the peptides Compound **26a** (14.6 mg, 15.4%), **26b** (6.67 mg, 8.7%) and **26c** (7.4 mg, 9.5%) as white powders. Compound **26a:** MS (MALDI-TOF) *m/z* calcd for $C_{106}H_{165}N_{38}O_{28}S_2$ ([M+H]$^+$): 2482.2, found 2482.5. Compound **26b**: MS (MALDI-TOF) *m/z* calcd for $C_{106}H_{165}N_{36}O_{28}S_2$ ([M+H]$^+$): 2454.2, found 2453.9. Compound **26c**: MS (MALDI-TOF) *m/z* calcd for $C_{111}H_{166}FN_{36}O_{28}S_2$ ([M+H]$^+$): 2534.2, found 2533.8.

#### 4.1.6. Indium chelating for CXCR4 antagonist probes (27a–c)

To a solution of peptides **26a–c** (8 mM in 0.1 N AcOH, **26a**: 45.9 μL, 0.37 μmol; **26b**: 48.4 μL, 0.39 μmol; **26c**: 48.8 μL, 0.39 μmol), $InCl_3$ (1 M in 0.02 N HCl, 50 μL) was added and the solution stirred for a further 30 min at room temperature. HPLC purification using a standard procedure provided the desired peptides **27a** (0.43 mg, 36.7%), **27b** (0.42 mg, 34.3%) and **27c** (0.38 mg, 30.3%) as white powders. Compound **27a**: MS (MALDI-TOF) *m/z* calcd for $C_{106}H_{165}InN_{38}O_{28}S_2$ ([M+H]$^+$): 2597.1, found 2596.9. Compound **27b**: MS (MALDI-TOF) *m/z* calcd for $C_{106}H_{165}InN_{36}O_{28}S_2$ ([M+H]$^+$): 2569.1, found 2569.1. Compound **27c**: MS (MALDI-TOF) *m/z* calcd for $C_{111}H_{166}FInN_{36}O_{28}S_2$ ([M+H]$^+$): 2649.1, found 2649.0.

### 4.2. Evaluation of [$^{125}$I]-SDF-1 binding and displacement

For ligand binding, the CXCR4 membrane was incubated with 0.5 nM of [$^{125}$I]-SDF-1 and increasing concentrations of compounds **27a–c** in binding buffer [50 mM HEPES (pH 7.4), 5 mM $MgCl_2$, 1 mM $CaCl_2$ and 0.1% BSA in $H_2O$] for 1 h at room temperature. The reaction mixtures were filtered through GF/B filters (Perkin-Elmer, Wellesley, MA) pretreated with 0.1% polyethyleneimine. The filter plate was washed with wash buffer [50 mM HEPES (pH 7.4), 500 mM NaCl and 0.1% BSA in $H_2O$] and the bound radioactivity was measured by TopCount (Packard, Meriden, CT). Inhibitory activity of test compounds was determined based on the inhibition of [$^{125}$I]-SDF-1 binding to the CXCR4 receptor ($IC_{50}$).


### Acknowledgments

This work is supported by Grants-in-Aid for Scientific Research and Molecular Imaging Research Program from the Ministry of Education, Culture, Sports, Science, and Technology of Japan. R.M. is grateful for Research Fellowships from the JSPS for Young Scientists.


### Supplementary data

Supplementary data associated with this article can be found, in the online version, at doi:10.1016/j.bmc.2011.03.059.

### References and notes


1. Lee, S.; Xie, J.; Chen, X. *Chem. Rev.* **2010**, *110*, 3087.
2. De León-Rodríguez, L. M.; Kovacs, Z. *Bioconjugate Chem.* **2008**, *19*, 391.
3. Mier, W.; Hoffend, J.; Krmer, S.; Schuhmacher, J.; Hull, W. E.; Eisenhut, M.; Haberkorn, U. *Bioconjugate Chem.* **2005**, *16*, 237.
4. Lewis, M. R.; Shively, J. E. *Bioconjugate Chem.* **1998**, *9*, 72.
5. Heppeler, A.; Froidevaux, S.; Mäcke, H. R.; Jermann, E.; Powell, P.; Henning, M. *Chem. Eur. J.* **1999**, *5*, 1974.
6. De León-Rodriguez, L. M.; Kovacs, Z.; Dieckmann, G. R.; Sherry, A. D. *Chem. Eur. J.* **2004**, *10*, 1149.
7. Wild, D.; Wicki, A.; Mansi, R.; Béhé, M.; Keil, B.; Bernhardt, P.; Christofori, G.; Ell, P. J.; Mäcke, H. R. *J. Nucl. Med.* **2010**, *51*, 1059, and the references therein.
8. De Jong, M.; Breeman, W. A.; Bakker, W. H.; Kooij, P. P.; Bernard, B. F.; Hofland, L. J.; Visser, T. J.; Srinivasan, A.; Schmidt, M. A.; Erion, J. L.; Bugaj, J. E.; Mäcke, H. R.; Krenning, E. P. *Cancer Res.* **1998**, *58*, 437.
9. Hnatowich, D. J.; Layne, W. W.; Childs, R. L. *Int. J. Appl. Radiat. Isot.* **1982**, *33*, 327.
10. Wang, S.; Luo, J.; Lantrip, D. A.; Waters, D. J.; Mathias, C. J.; Green, M. A.; Fuchs, P. L.; Low, P. S. *Bioconjugate Chem.* **1997**, *8*, 673.
11. Reilly, R.; Lee, N.; Houle, S.; Law, J.; Marks, A. *Appl. Radiat. Isot.* **1992**, *43*, 961.
12. Hnatowich, D. J.; Layne, W. W.; Childs, R. L.; Lanteigne, D.; Davis, M. A.; Griffin, T. W.; Doherty, P. W. *Science* **1983**, *220*, 613.
13. Van Hagen, P. M.; Breeman, W. A. P.; Bernard, H. F.; Schaar, M.; Mooij, C. M.; Srinivasan, A.; Schmidt, M. A.; Krenning, E. P.; De Jong, M. *Int. J. Cancer* **2000**, *90*, 186.
14. Arano, Y.; Uezono, T.; Akizawa, H.; Ono, M.; Wakisaka, K.; Nakayama, M.; Sakahara, H.; Konishi, J.; Yokoyama, A. *J. Med. Chem.* **1996**, *39*, 3451.
15. A portion of this study was reported in a preliminary communication: Masuda, R.; Ohno, H.; Oishi, S.; Fujii, N. In *Pepide Science*, Okamoto, Ed.; 2009, p 159.
16. Peterson, J. J.; Pak, R. H.; Meares, C. F. *Bioconjugate Chem.* **1999**, *10*, 316.
17. Hidai, Y.; Kan, T.; Fukuyama, T. *Chem. Pharm. Bull.* **2000**, *48*, 1570.
18. Arano, Y.; Akizawa, H.; Uezono, T.; Akaji, K.; Ono, M.; Funakoshi, S.; Koizumi, M.; Yokoyama, A.; Kiso, Y.; Saji, H. *Bioconjugate Chem.* **1997**, *8*, 442.
19. Lewis, J. S.; Anderson, C. J. *Methods Mol. Biol.* **2007**, *386*, 227.
20. Albert, R.; Smith-Jones, P.; Stolz, B.; Simeon, C.; Knecht, H.; Bruns, C.; Pless, J. *Bioorg. Med. Chem. Lett.* **1998**, *8*, 1207.
21. Müller, A.; Homey, B.; Soto, H.; Ge, N.; Catron, D.; Buchanan, M. E.; McClanahan, T.; Murphy, E.; Yuan, W.; Wagner, S. N.; Barrera, J. L.; Mohar, A.; Verástegui, E.; Zlotnik, A. *Nature* **2001**, *410*, 50.
22. Hermann, P. C.; Huber, S. L.; Heeschen, C. *Cell Cycle* **2008**, *7*, 188.
23. Oishi, S.; Masuda, R.; Evans, B.; Ueda, S.; Goto, Y.; Ohno, H.; Hirasawa, A.; Tsujimoto, G.; Wang, Z.; Peiper, S. C.; Naito, T.; Kodama, E.; Matsuoka, M.; Fujii, N. *ChemBioChem* **2008**, *9*, 1154.
24. Nishizawa, K.; Nishiyama, H.; Oishi, S.; Tanahara, N.; Kotani, H.; Mikami, Y.; Toda, Y.; Evans, B. J.; Peiper, S. C.; Saito, R.; Watanabe, J.; Fujii, N.; Ogawa, O. *Int. J. Cancer* **2010**, *127*, 1180.
25. Hanaoka, H.; Mukai, T.; Tamamura, H.; Mori, T.; Ishino, S.; Ogawa, K.; Iida, Y.; Doi, R.; Fujii, N.; Saji, H. *Nucl. Med. Biol.* **2006**, *33*, 489.
26. Tamamura, H.; Omagari, A.; Oishi, S.; Kanamoto, T.; Yamamoto, N.; Peiper, S. C.; Nakashima, H.; Otaka, A.; Fujii, N. *Bioorg. Med. Chem. Lett.* **2000**, *10*, 2633.
27. Stephenson, K. A.; Banerjee, S. R.; McFarlane, N.; Boreham, D. R.; Maresca, K. P.; Babich, J. W.; Zubieta, J.; Valliant, J. F. *Can. J. Chem.* **2005**, *83*, 2060.
28. Tamamura, H.; Hiramatsu, K.; Mizumoto, M.; Ueda, S.; Kusano, S.; Terakubo, S.; Akamatsu, M.; Yamamoto, N.; Trent, J. O.; Wang, Z.; Peiper, S. C.; Nakashima, H.; Otaka, A.; Fujii, N. *Org. Biomol. Chem.* **2003**, *1*, 3663.

# 1. 悪性腫瘍の分子イメージングのための新しい分子プローブの設計

[1)]京都大学医学部附属病院 RI 実験施設、[2)]京都大学大学院薬学研究科　上田真史[1)]・天滿敬[2)]・佐治英郎[2)]

## 1．はじめに

悪性腫瘍を対象とした分子イメージングプローブである $^{18}$F-FDG は、腫瘍の病期診断、再発・転移診断など、主として腫瘍の存在の有無やサイズを評価するために用いられている。一方で、浸潤・転移能や治療反応性など、腫瘍の性質は非常に多様性に富むことが知られており、腫瘍の性状把握・質的診断を可能とする分子イメージングプローブがポスト FDG として期待されている。また近年、抗体医薬・タンパク医薬の発展には目覚しいものがあり、抗体やタンパク質・ペプチドの高い生理活性に着目してそれらを母体とした分子プローブ開発も注目を集めている。

## 2．機能性ユニットカップリング型分子プローブ

$^{18}$F-FDG は $^{18}$F 標識されたブドウ糖類似体であり、$^{11}$C-PIB は β アミロイド結合性を有するチオフラビン T 類似体の $^{11}$C 標識体である。このように従来のイメージングプローブは、目的とする性質を有する化合物に RI 標識を施したある一つのかたまり（単一分子）として捉えられるのが一般的であった。これに対し我々は、イメージングプローブを「標的認識ユニット」「リンカーユニット」「シグナル放出ユニット」の各ユニットの集合体として捉える「機能性ユニットカップリング型分子プローブ」という新概念に基づく分子プローブ設計を行っている（図 1）。この方法では、イメージング対象に発現している標的分子や利用する撮像装置に応じて最適なユニットを選択することで、種々のイメージング標的・装置に対応可能な汎用性の高い分子プローブの開発が可能となる。さらに、「標的認識ユニット」と「クリアランスの速い低分子シグナル放出ユニット」のカップリングをインビボ（*in vivo*）で行うことにより体内動態を制御し、投与早期での高コントラスト画像の取得・被ばく線量の低減を実現することもできる。本稿ではこの概念に基づいて設計した、膜結合型マトリクス分解酵素（membrane type 1 matrix metalloproteinase;

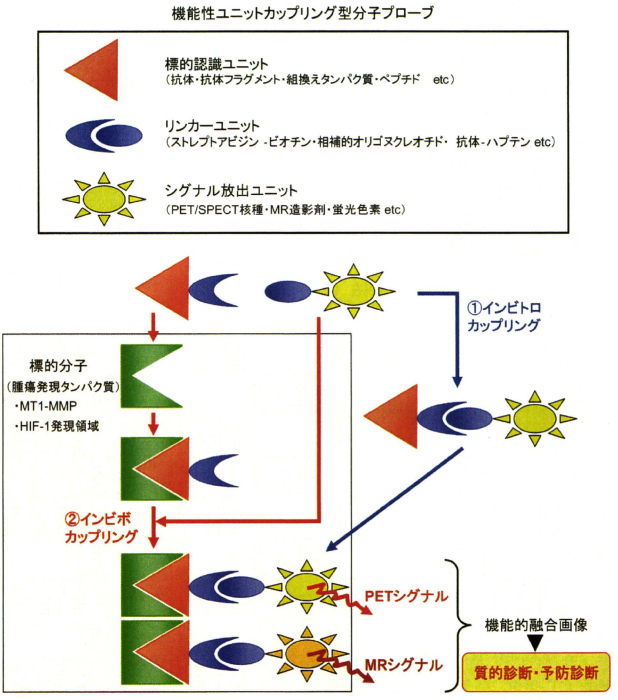


図1　機能性ユニットカップリング型プローブを利用したイメージングの概念図

MT1-MMP）標的イメージングプローブおよび低酸素誘導因子（hypoxia-inducible factor-1; HIF-1）存在領域イメージングプローブの研究成果を紹介する。

### 3. MT1-MMP 標的分子イメージングプローブの開発

MT1-MMPは、乳がんを始めとした種々の腫瘍においてMMP-2の活性化を介した悪性度との高い連関性が示されている。さらに、分泌型酵素であるMMP-2とは異なり、膜結合型でその発現が腫瘍細胞の細胞膜上に限局していることから、腫瘍の存在位置を確実に把握しつつ悪性度診断（質的診断）を同時に行うことができる非常に有望なイメージング標的分子である。

MT1-MMPをイメージングするため、我々は、当該タンパク質の細胞膜外領域に存在し、生体内での3次元構造・代謝調節機構を踏まえ認識されやすいと考えられるペプチド配列をエピトープとする抗MT-1MMPモノクローナル抗体（mAb）を標的認識ユニットとして選択した[1]。さらに、ストレプトアビジン－ビオチンの高親和性結合に着目し、ストレプトアビジン（SAV）をリンカーユニットとして抗体に導入したプローブanti-MT1-MMP mAb-SAVを構築し、それに結合性を有するシグナル放出ユニットである放射性ヨウ素標識ビオチン誘導体（3-[123/125I]iodobenzoyl)norbiotinamide; $^{123/125}$I-IBB）の合成も行った。まず、インビトロカップリングにより両者を直接結合させたプローブを用いて標的認識ユニットの有効性を評価したところ、MT1-MMP発現細胞に高く取り込まれること、インビボで腫瘍集積性を示すことを見出し、選択した抗体が標的認識ユニットとして有効に機能することを明らかとした。次に、抗体の血液クリアランスの遅さを克服し、投与早期で良好な画像コントラストを達成するため、anti-MT1-MMP mAb-SAVを投与してから72時間後に$^{125}$I-IBBを投与するインビボカップリングを検討したところ、投与3時間後における腫瘍血液比は直接結合体（インビトロカップリング）の場合の30倍以上であることを認めた[2]。そこで、$^{123}$I-IBBを投与後、SPECTを用いて経時的に撮像を行ったところ、投与3時間後から明瞭に腫瘍が描出された（**図2**）[2]。さらに、免疫組織化学的検討の結果、腫瘍内の放射能局在はMT1-MMP発現部位と一致することを認めた。これらの結果から、ユニットカップリング型プローブの設計概念に基づいて構築したanti-MT1-MMP mAb-SAVと$^{123}$I-IBBを用いてインビボカップリングSPECT撮像を行うことにより、MT1-MMP発現腫瘍の投与早期イメージングが可能となることを見出した。

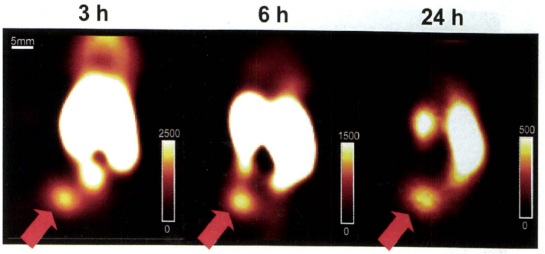


図2　インビボカップリング法によるMT1-MMP発現腫瘍の経時的SPECT画像
（矢印が腫瘍で、投与3時間後から明瞭に描出されている）

### 4. HIF-1 存在領域イメージングプローブの開発

HIF-1は低酸素領域でのみ安定に存在する転写因子であり、糖代謝・血管新生・浸潤・転移に関与する種々のタンパク質発現を亢進させて腫瘍の悪性化や治療抵抗性に関与することが知られていることから、腫瘍内でのHIF-1存在量やその局在を同定できる分子プローブが開発できれば、腫瘍の性状把握・悪性度診断・予後予測に有用な情報を得ることが可能となる。また、HIF-1が安定に存在しうる酸素分圧の閾値は一定ではなく、組織によって異なることが報告されている。すなわちHIF-1は、生体組織が酸素不足を感じる生物学的低酸素領域に存在しており、その領域は酸素分圧が10 mmHg以下のいわゆる物理的低酸素領域と完全には一致しないことから、$^{18}$F-FMISOなど既存の低酸素プローブとは別のコンセプトに基づくプローブ開発が必要となる。

HIF-1はαサブユニット（HIF-1α）とβサブユニットからなる転写因子で、通常酸素環境下ではHIF-1αは分解される一方、低酸素環境下では安定に存在することで転写活性を調節して

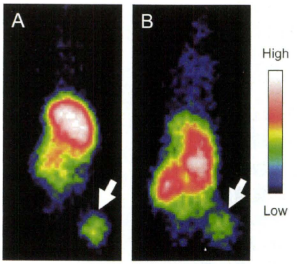


図3　POSと$^{123}$I-IBBを用いたインビトロカップリング法（A：投与24時間後）およびインビボカップリング法（B：投与6時間後）による腫瘍内HIF-1存在領域（矢印）のプラナー画像

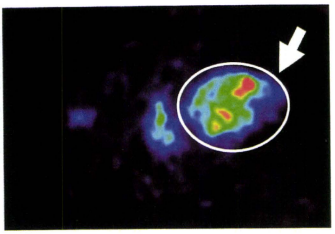

図4　インビボカップリング法による腫瘍内 HIF-1 存在領域（矢印）の PET 画像（投与 3 時間後に撮像）

いる。そこで我々はその分解機構に着目し、HIF-1α と同じメカニズムで分解・安定化の制御を受けるプローブを構築し、HIF-1 存在領域のイメージングの可能性について検討を行った。

HIF-1α の通常酸素環境下での分解には、タンパク質中の酸素依存的分解配列（oxygen-dependent degradation domain; ODD）が関与することが報告されている。そこで、ODD の中でも酸素依存的分解制御に必須のアミノ酸配列を選別し、それに細胞膜透過配列（protein transduction domain; PTD）および SAV 単量体を融合させた新規タンパク質 PTD-ODD-SAV（POS）を構築した。POS と $^{125}$I-IBB をインビトロカップリングさせて細胞に処置したところ、通常酸素環境下（20%$O_2$）よりも低酸素環境下（0.1%$O_2$）で高い放射能集積を認めた。また、担がんマウスに投与して体内動態を検討したところ、投与 24 時間後で明瞭な腫瘍の画像化に成功し（図 3A）、そのときの放射能集積量および局在が HIF-1 転写活性や存在領域と一致することを認めた[3]。これらの結果から、POS が HIF-1 存在領域を対象とした標的認識ユニットとして有効に機能することが明らかとなった。

そこで次に、投与早期における HIF-1 存在領域イメージングを達成するためのインビボカップリング法の利用について検討を行った。POS を担がんマウスに投与し、インビトロカップリングの際に明瞭に腫瘍が描出された 24 時間後から $^{125}$I-IBB を投与し、体内動態を経時的に調べたところ、投与 6 時間後で腫瘍に集積した放射能は非投与群の 30 倍以上であった。また、その集積は過剰量のビオチン投与によって抑制されたことから、$^{125}$I-IBB が所期の通り、POS の SAV 部分とインビボでカップリングすることが示された[4]。さらに、$^{123}$I-IBB を投与後、経時的にプラナー撮像を行ったところ、投与 6 時間後で明瞭に腫瘍が描出された（図 3B）[4]。これは、インビトロカップリングさせたプローブを投与してから 24 時間後と同等のコントラストの画像であり、POS と $^{123}$I-IBB を用いるインビボカップリング法により、腫瘍内 HIF-1 存在領域の投与早期イメージングが可能となることを見出した。

このように、投与早期に高コントラスト画像を得られるイメージング法は、短半減期核種の利用が多い PET においては高い有効性が期待される。そこでこの概念を PET に応用すべく、放射性フッ素標識ビオチン誘導体（(4-[$^{18}$F]fluorobenzoyl)norbiotinamide; $^{18}$F-FBB）を新規に設計・合成し、インビボカップリング PET に関する検討を行った。POS 投与 24 時間後に $^{18}$F-FBB を投与して体内動態を経時的に調べたところ、投与 3 時間後で非投与群の 20 倍以上の放射能が腫瘍に集積し、その集積は過剰量のビオチン投与によって 80%以上抑制された。PET 撮像を行ったところ、投与 3 時間後で明瞭に腫瘍が描出され（図 4）、その放射能集積量および局在が HIF-1 転写活性や存在領域と一致することを認めた[5]。このようにインビボカップリング法は、短半減期核種を利用する PET の場合でも有効に機能することが明らかとなった。

## 5. おわりに

本稿では、「機能性ユニットカップリング型分子プローブ」の概念とその実用例として、腫瘍の転移能や低酸素状態といった性状を把握しうる分子プローブを紹介した。今後、この概念に基づき、多種多様ながんの性状それぞれを把握し得る「標的認識ユニット」および各モダリティに対応した「シグナル放出ユニット」を組み合わせることで、がんの性状をマルチモーダルに捉え得る分子プローブの効率的な開発が可能となる。それらの分子プローブは、悪性腫瘍の存在を単に検出するのみならず、質的診断に基づく治療方針の最適化にも大きく貢献することが期待できる。

## 6. 文献

1) Temma T, et al: Biol Pharm Bull **32**: 1272–1277, 2009
2) Sano K, et al: Biol Pharm Bull **33**: 1589–1595, 2010
3) Kudo T, et al: J Nucl Med **50**: 942–949, 2009
4) Ueda M, et al: Eur J Nucl Med Mol Imaging **37**: 1566–1574, 2010
5) Kudo T, et al: Mol Imaging Biol, in press

# 2. 冠動脈プラークの分子イメージング

京都大学大学院薬学研究科病態機能分析学分野教授　佐治英郎
同　病態機能分析学分野　天滿　敬

**key words**　molecular imaging, atherosclerosis, plaque, PET, SPECT, nuclear medicine, FDG, LOX, apoptosis, MMP

**動　向**

冠状動脈において，動脈硬化病巣に脂質が沈着してできる不安定プラーク（粥腫）が破綻すると，血栓形成，血管内腔の狭窄・閉塞という一連の病態を引き起こし，急性冠症候群の原因となる．したがって，不安定プラークを検出することは臨床的に重要であり，そのためには形態的情報と質的情報（生化学，細胞生物学的変化に関する情報）とを得ることが有効である．これまでに，CT，MRIなどの進歩により解像力の高い形態学的な情報が得られるようになっている．そこで，最近急速に発展してきた，細胞/分子レベルの生化学・細胞生物学的なプロセス（事象）の空間的・時間的分布をin vivoで画像化する分子イメージングを用いて不安定プラークの質的情報を得，これを上記の形態情報と組み合わせることにより，不安定プラークの優れた診断が可能となることが期待されている[1-4]．

## A. 動脈硬化プラークと分子イメージング

動脈硬化病巣には脂質が沈着してできるプラーク（粥腫）が認められるが，このプラークには，破綻しにくい安定なものと，破綻しやすい不安定なものとが存在する．不安定プラークは，プラークの破綻，血栓形成，血管内腔の狭窄・閉塞という一連の病態を引き起こし，急性冠症候群や脳塞栓症の原因となる[1]（図1）．したがって，不安定プラークを特異的に検出することができれば，急性冠症候群や脳塞栓症に繋がる動脈硬化の臨床診断，動脈硬化の治療効果の評価，梗塞性疾患発症の予防的治療を行うことが可能となる．

この不安定プラークの特徴として，①脂質に富む柔らかな粥腫があること，②線維性被膜が脆弱化していること，③マクロファージなどの炎症性細胞が浸潤しているなどのことが挙げられる（図1）．これに対し，安定プラークでは線維性組織が発達し内膜の肥厚は認められるものの，粥腫も小さく，線維性被膜も厚く，マクロファージの浸潤はほとんどない．

現在，一般的に行われているX線CTによる冠動脈造影では，血管の狭窄度を測定することが可能である．しかし，動脈硬化性病変部では動脈硬化の初期には血管内腔が保たれて冠血管体が外側に向かって代償性に拡大し，動脈硬化が全血管面積の約40%を超えると内腔の狭小化が始まるという，血管自体の代償性拡大が起こることが知られている．したがって，軽度の動脈硬化は冠動脈

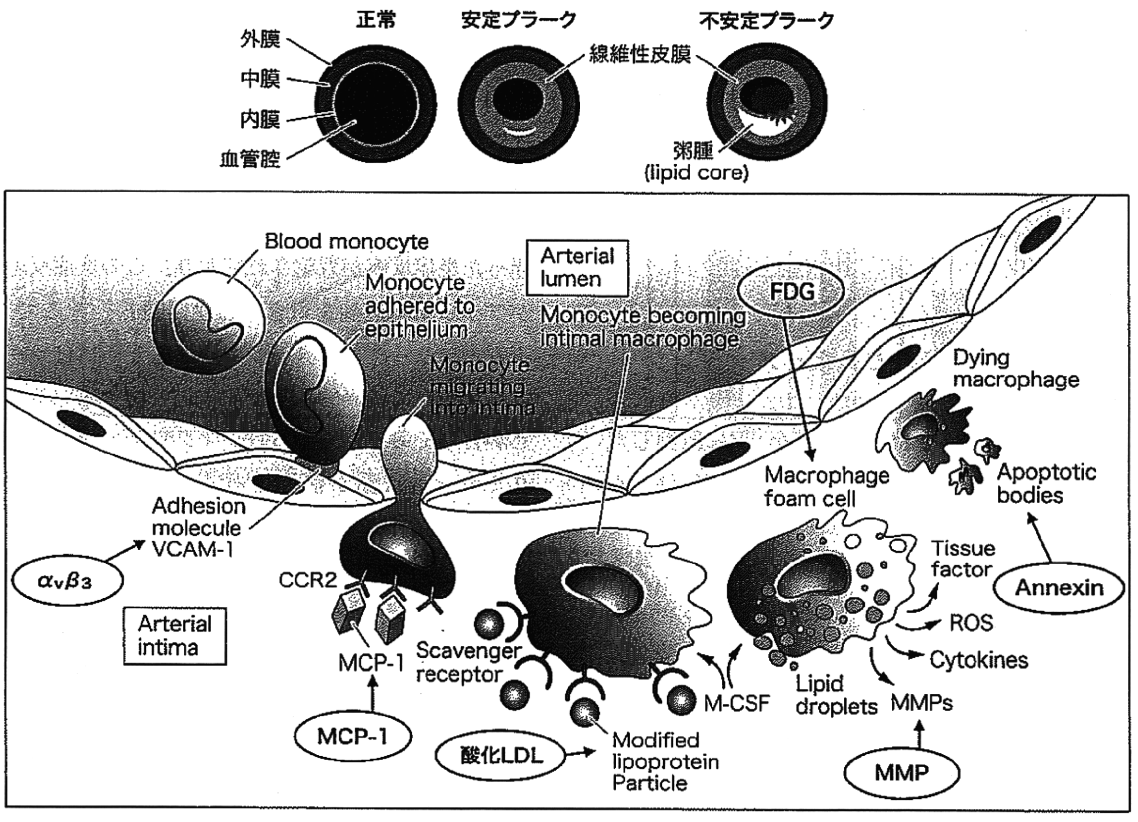


**図1　動脈硬化プラークの形成と破壊過程とそれに関与する因子**（文献1より改変）

造影で評価できない．また，急性心筋梗塞に至った病変の約70%は狭窄率50%以下の病変であり，梗塞責任病巣の80～90%は狭窄率70%以下であるとの報告もある．これらのことから，動脈の狭窄度よりもむしろ病変部に存在するプラークの質を診断して不安定か安定かを見極めることが，早期診断，早期治療のために重要と考えられる．最近，超音波診断法やMRIといった形態学的診断法による不安定プラークの検出が試みられているが，その性状に関する鑑別は熟練を必要とし，また，定量的に不安定性を評価するには至っていない．これに対し，PET（positron emission tomography），SPECT（single photon emission computed tomography）等の核医学画像法を用いれば，不安定プラークの機能変化を把握することができ，その質的診断が可能となると考えられる．

一方，最近，進歩が著しい生体画像工学と分子・細胞生物学の成果を融合させて，生化学・生物学・臨床診断・治療に適用するために細胞/分子レベルの生化学・細胞生物学的なプロセス（事象）の空間的・時間的分布をin vivoで画像化する，「分子イメージング」という領域が開拓され，ライフサイエンスの基礎研究，生体機能や病因の解明研究，創薬研究などへの貢献とともに，臨床診断分野への応用が疾患の質的診断に繋がるものとして期待されている．

そこで，動脈硬化プラークの臨床診断の分野においても分子イメージングによる質的診断が期待され，PET，SPECT等の核医学画像法を中心に，

炎症および血管リモデリングに関与するマクロファージの代謝活性や表面に存在するスカベンジャー受容体，蛋白分解酵素（MMPなど），酸化LDL，血管新生に関与する細胞接着因子，アポトーシスなどを標的とする動脈硬化不安定プラークの分子イメージング研究が活発に行われている[1-6]（図1）．

## B. 代謝活性を標的としたイメージング

D-グルコースの2位の水酸基を$^{18}$Fに置換した$^{18}$F-フルオロデオキシグルコース（FDG）はグルコースと同様にグルコーストランスポータ（GLUT）により細胞内に取り込まれ，ヘキソキナーゼ（HK）によって6-リン酸化されるが，生成したFDG-6-リン酸がそれ以後の解糖系酵素の基質とならないため，細胞内に滞留する（図2）．この$^{18}$F-FDGは，腫瘍，心筋虚血，脳のてんかん焦点などの検出，化学療法や放射線療法に対する反応性や治療効果の予測などにおける有効性が多くの臨床データによって明らかにされており，$^{18}$F-FDGイメージングは現在分子イメージングの代表的なものとなっている．

不安定プラークでは薄い線維性皮膜の内側に脂質を含む粥腫が蓄積し，マクロファージの浸潤を伴った炎症反応が惹起されており，この炎症反応がプラークの破綻を引き起こす（図1）．そこで，不安定プラークをイメージングするためにはマクロファージに特異的に集積する化合物を用いることが有効であると考えられ，マクロファージではグルコース代謝が活発であることに着目して，$^{18}$F-FDGによる不安定プラークのイメージングが基礎的および臨床的に検討されている．

すなわち，ヒトの場合と類似した動脈硬化病変を示すWHHLMIウサギ（myocardial infarction-prone Watanabe heritable hyperlipidemic rabbit）を用いた検討において，WHHLMIウサギの血管には，動脈硬化を起こしていない対照群

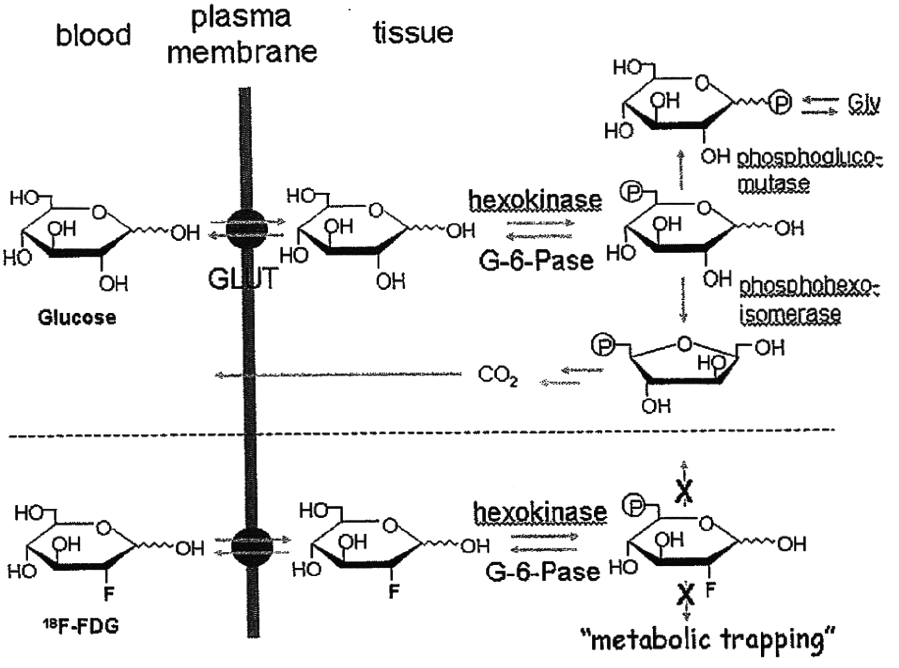


図2　静脈投与された$^{18}$F-FDGの組織への集積機構

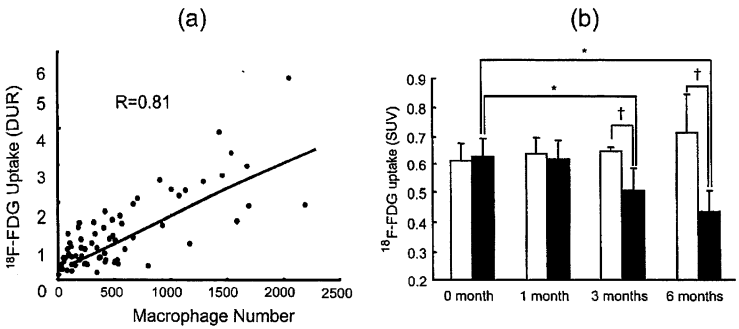


**図3　a: WHHLMIウサギの大動脈血管壁でのマクロファージ数と$^{18}$F-FDG集積量との関係,**
**b: 動脈硬化治療薬投与後のWHHLMIウサギの大動脈血管壁への$^{18}$F-FDG集積量の経時的変化**
□Control group, ■Probucol group, *$p < 0.05$ vs 0 month, †$p < 0.05$ vs control

のNew Zealand Whiteウサギの血管に比較して，有意に高い$^{18}$F-FDGの集積を認め，また，その集積量はマクロファージ数と高い相関があることが示されている（図3）．一方，内膜の肥厚度と$^{18}$F-FDGの集積量の間には相関は認められなかったことから，$^{18}$F-FDGを用いることにより，プラーク不安定性の指標となるマクロファージの浸潤度を対象として，不安定プラークを描出できることが示されている[7]．実際，臨床でも$^{18}$F-FDGによって不安定プラークがイメージングできることが報告されている[2,3,8-10]．

また，ある種のスタチン化合物は血中コレステロール濃度を低下させるが，マクロファージの浸潤量は減少させないことから，薬物治療時での$^{18}$F-FDGによる不安定プラークの質的評価は，治療方針決定や新しい治療薬開発に有効な情報を与えることが期待される．実際，動脈硬化治療薬を投薬したWHHLウサギの$^{18}$F-FDG-PET撮像を行い，動脈硬化病巣を有する血管への放射能の集積量を検討した結果，それはマクロファージ数の低下に一致して低下した(図3b)[11-13]．実際，$^{18}$F-FDG-PET法は新規開発の動脈硬化治療薬の治験の場合の画像バイオマーカーとして使用されている場合もある[14]．なお，$^{18}$F-FDGの取り込みは，動脈硬化治療薬の投与だけでなく，ダイエット，生活習慣の変化によっても減少することも示されているので，評価には注意が必要である[15]．

また，活性化マクロファージでは増殖活性のために細胞膜を構築する過程が増加し，細胞膜の構成成分であるコリンの取り込みが増加していることに着目して，$^{18}$Fで標識されたコリン誘導体フルオロコリン($^{18}$F-FCH)が不安定プラークイメージングプローブとして検討され，本プローブは$^{18}$F-FDGよりも短時間で，かつ高い検出感度で不安定プラークをイメージングできると報告されている[16]．

## C. 酸化LDL受容体を標的としたイメージング

酸化LDL受容体であるlectin-like oxidized LDL receptor-1（LOX-1）は，i) LOX-1が酸化